Eshelby-Mori-Tanaka approach for post-buckling analysis of axially compressed functionally graded CNT/polymer composite cylindrical panels

Enrique García-Macías[a,*], Luis Rodríguez-Tembleque[a], Rafael Castro-Triguero[b], Andrés Sáez[a]

[a] *Department of Continuum Mechanics and Structural Analysis, School of Engineering, University of Seville , Camino de los Descubrimientos s/n, E-41092-Seville, Spain*

[b] *Department of Mechanics, University of Córdoba, Campus de Rabanales, Cordoba, CP 14071, Spain*

Abstract

Carbon nanotubes have drawn enormous attention in recent years due to their outstanding mechanical and multifunctional properties. In addition, the growing tendency of aeronautical engineering to incorporate advanced composite materials in aircraft structures suggests carbon nanotube reinforced composites as ideal materials for high-performance fuselage panels. Nevertheless, due to the theoretical difficulties in the underlying differential problem induced by curvature, along with the technology of carbon nanotube based composites that is still under development, the number of research works on the post-buckling behavior of carbon nanotube reinforced composite curved panels is still scant. Furthermore, numerous experimental results in the literature report about the wavy state of nanotubes in polymer matrices, as well as their tendency to gather in bundles due to their high van der Waals force attraction. Therefore, advanced homogenization approaches are needed to account for these phenomena and assist the structural design. In this context, this paper presents detailed parametric analyses of the post-buckling behavior of functionally graded carbon nanotube reinforced curved panels under uniaxial compression. In particular, the effects of filler content, fiber orientation, distribution along the thickness, and misalignment of fibers are investigated. To this aim, the overall elastic moduli of carbon nanotube reinforced composites are computed by the Eshelby-Mori-Tanaka method with consideration of waviness and agglomeration effects. The presented results prove the essential role of the micromechanical variables in the design of high-strength composite curved panels. Notably, the theoretical simulations highlight the detrimental effect of waviness and agglomeration on the mechanical response of these composites. In light of this study, it is concluded that the incorporation of the considered micromechanical variables is essential for the study of the post-buckling response of functionally graded carbon nanotube reinforced curved panels under axial compression.

Keywords:
Agglomeration, Cylindrical panel, Functionally graded carbon nanotube, Orientation Distribution Function, Waviness

1. Introduction

Over the last decades, the usage of fiber-reinforced composites is steadily rising in diverse fields such as sports equipment, automotive or aerospace engineering. A paradigmatic example is the recently developed commercial aircraft Boeing 787, in which half of the weight was designed with composite materials, mainly carbon fiber reinforced plastics [1]. This growing tendency to use composites for lightweight high-performance applications has encouraged researchers to study micro- and nano-scale fillers. In particular, Carbon Nanotubes (CNTs) have drawn much attention due to their remarkable physical-mechanical properties as reinforcing fibers [2], and smart materials with self-sensing properties [3]. A fascinating range of novel applications stems from these coupled features with the development of high-strength and lightweight structural elements which, at the same time, exhibit self-sensing piezoresistive capabilities apt for Non-Destructive Evaluation (NDE) and Structural Health Monitoring (SHM) [4–9]. The application of CNTs as reinforcements in Functionally Graded Materials (FGM) shows promise for developing tailor-made structural elements that meet superior load-bearing requirements. These advanced materials are defined by spatially continuous varying properties, such as gradation of doping concentration or orientation across the thickness [10]. Unlike laminated materials, FGMs exhibit smooth and continuous variations of their material properties and, therefore, prevent delamination and debonding failures caused by stress

*Corresponding author.
Email address: egarcia28@us.es (Enrique García-Macías)

concentrations at interfaces [11, 12]. A potential application of Functionally Graded CNT Reinforced Composites (FG-CNTRCs) is the design of curved lightweight fuselage panels. In order to maximize the strength to weight ratio of these panels, it is often necessary to allow the panel to buckle below the ultimate failure load. The study of the post-buckling behavior is thus crucial for the application of FG-CNTRC aircraft structures. Nevertheless, works in this regard are still limited in the literature.

There exists a variety of works on the linear elastic buckling analysis of curved panels. The first analytical solutions for the buckling of isotropic curved panels under axial compression and simply supported edges were those by Redshaw [13] and Timoshenko [14]. Different edge-support conditions were also taken into account by Stowell [15] who proposed a modified form of Redshaw's expression. Nevertheless, owing to the complexity inherent in the underlying differential problem, more accurate solutions of the critical buckling loads of curved panels need the use of numerical approaches. It is worth noting the work by Le Tran *et al*. [16] who proposed semi-empirical formulae for predicting the elastic buckling and ultimate strength of curved panels on the basis of finite element simulations. The critical loads computed by the aforementioned techniques are based on the solution of the linear eigenvalue problem. Hence, the critical loads are defined as those for which the model stiffness becomes singular. In real structures, these critical loads are generally much higher than the actual buckling loads [17, 18], causing linear design calculations to be non-conservative. In practice, most standards prescribe knock-down factors to provide better approximations. Many theoretical investigations have reported about more accurate non-linear buckling analyses. Among them, one of the first investigations is the one published by Cox and Pribam [19] who used a semi-empirical energy approach to qualitatively analyze the post-buckling behavior of axially compressed panels. That work showed that, similarly to the case of complete cylinders [20], a degree of unloading and shortening occurs immediately after buckling. Koiter [21, 22] proposed a perturbation approach which, in the special case of axially compressed cylindrical panels, reveals a substantial sensitivity of buckling loads to initial geometrical imperfections. Similar conclusions were also reached by Pope [23] who used the principle of virtual work to determine the equilibrium path of simply supported infinitely-long shallow cylindrical panels. In that work, it was shown that increasing curvature values induce a twofold effect: (i) significant increase of the linear buckling load and (ii) reduction of the post-buckled tangent stiffness. Other widely used approaches for performing nonlinear post-buckling analyses of shell structures are path following schemes. These include the Newton-Raphson methods which were initially attractive for solving large nonlinear systems. However, these approaches usually lose convergence at limit points and can not trace the unstable equilibrium paths. Riks [24] proposed a more efficient arc-length method that can trace both stable and unstable post-buckling equilibrium paths. Modified versions were also proposed by Crisfield [25] and Tsai *et al*. [26] to handle more complicated post-buckling behaviors. Despite many efforts have been made, the post-buckling response of curved panels remains a subject of active research.

The number of studies into the post-buckling behavior of composite curved panels is more limited. Bauld and Khot [27] conducted experiments on the buckling behavior of axially compressed, fiber-reinforced laminate $[0, 90]_{2s}$ cylindrical panels. The experimental results were compared with numerical predictions from a Rayleigh-Ritz and finite-difference approach. The authors first computed the equilibrium paths accounting for perfect cylindrical geometries and small axially symmetric initial imperfections and, afterward, using experimentally measured transverse imperfections [28]. Zhang and Mathews [29, 30] investigated the post-buckling behavior of generally layered composite curved panels by the use of non-linear Fourier series. An interesting remark of that work concerns the post-buckling behavior of asymmetric mid-plane stacking sequences. The prebuckling deformation of such panels is non-linear due to the bend-twist coupling and, thus, the bifurcation buckling does not exist when subjected to in-plane compression. Madenci and Barut [31] investigated laminated panels with cutouts under compression using non-linear finite element analysis. It is worth noting the more recent works of Hilburger *et al*. [32–34] that cover the numerical and experimental evaluation of the post-buckling behavior of isotropic curved panels, laminated panels, panels with cutouts, under different boundary conditions and loading conditions. White *et al*. [35] presented numerical results of the post-buckling response of variable stiffness cylindrical panels.

In particular, the number of investigations on the post-buckling of CNTRC and FG-CNTRC structural elements is still limited although steadily rising in more recent years. A notable example is the work by Shen and Zhang [36] who reported about the thermal buckling and post-buckling behavior of FG-CNTRC plates under in-plane temperature variation. Their results on perfect and imperfect plates showed that CNT distribution along the thickness can tailor the buckling temperature and thermal post-buckling strength. Zhu *et al*. [37] proposed a meshless local Petrov-Galerkin based on the moving Kriging interpolation technique for the nonlinear thermoelastic analysis of FG ceramic-metal plates in thermal environments. It is noteworthy the work of Lei *et al*. [38] who proposed a meshless kp-Ritz method for the dynamic stability analysis of FG-CNTRC cylindrical panels subjected to static and periodic axial forces. Shen and Xiang [39] employed a two-step perturbation approach to investigate the post-buckling behavior of FG-CNTRC cylindrical panels resting on Pasternak elastic foundations. A similar work was presented by Zhang *et al*. [40] who developed a meshless IMLS-Ritz method to evaluate the post-buckling behav-

ior of FG-CNTRC plates with edges elastically restrained against translation and rotation. It is also worth noting the recent work of Shen *et al*. [41] who analyzed the post-buckling hehavior of graphene-reinforced composite laminated plates.

Among the different homogenization techniques available in the literature, the rule of mixtures [42] is the most widely used approach to evaluate the effective properties of CNTRCs. The simplicity of this approach has favored its use for a large number of studies of FG-CNTRC structural elements (e.g. [39, 43–47]). However, the theory of mixtures is restricted to the ideal configuration of uniaxially aligned and perfectly dispersed straight fibers which, in practice, may be highly unlikely. First, good fiber dispersions are difficult to obtain due to the tendency of CNTs to agglomerate in bundles. This effect is attributed to the electronic configuration of CNT walls and their high specific surface area which increases the van de Waals (vdW) attraction forces among nanotubes [48, 49]. Secondly, due to their large aspect ratio and very low bending stiffness, nanotubes usually exhibit a certain degree of waviness [50–53]. Although experimental results have extensively reported about these effects, the number of studies on FG-CNTRC structural elements that incorporate them is still rather scant. In this regard, the Eshelby-Mori-Tanaka approach [54] offers more possibilities to take into account micromechanical and morphological features of fillers. It is worth noting the work by Tornabene *et al*. [55] who investigated the effect of agglomeration on the natural frequencies of FG-CNTRC doubly-curved shells. To this aim, the authors used the two-parameter agglomeration model presented by Shi *et al*. [56] based on the classical Eshelby-Mori-Tanaka homogenization method. Their results showed that agglomeration has a detrimental effect on the overall stiffness what leads to substantial reductions of the natural frequencies. Tornabene and co-authors [57] also utilized this methodology to assess the effect of agglomeration on the linear static response of CNT reinforced laminated plates and shells. Similar recent approaches can be found in the literature on the study of FG-CNTRC structural elements [58, 59], effects of waviness [60], and agglomeration [61, 62].

This paper focuses on the post-buckling analysis of uniaxially loaded FG-CNTRC curved panels. In light of the state of art outlined above, the influence of micromechanical aspects such as fiber orientation, fiber orientation distribution, waviness and agglomeration is rather unexplored. This paper is aimed to shed some light on the effects of these variables on the mechanical response of FG-CNTRC curved panels. The panels have been modeled with the commercial FEA software ANSYS.0, and the effective properties of the composites have been estimated by means of a micromechanics model based on the Eshelby-Mori-Tanaka approach. Most research studies assume that CNTs are fully aligned or randomly oriented throughout the matrix. Unless special aligning techniques are undertaken (see e.g. [63]), CNTs are typically found randomly distributed in the matrix. Nonetheless, in real CNT/polymer nanocomposites, the manufacturing process induces complicated flow fields so that fillers may exhibit orientation distributions between the two limit cases, random and fully aligned. In this regard, this work also takes account of statistical CNTs orientation distributions in the determination of the macroscopic properties of these composites. Detailed parametric studies have been carried out to inspect the influence of fiber content, fiber angle, fiber distributions across the thickness, misalignment of fibers, waviness and agglomeration. The results show a substantial influence of these variables on the post-buckling behavior of FG-CNTRC curved panels. This research work, in conjunction with our previous paper [64], is envisaged to provide a useful approach for analyzing complex fiber orientations, including waviness and agglomeration effects, as well as valuable results for the design of high-performance FG-CNTRC curved fuselage panels.

The paper is organized as follows. Section 2 introduces the terminology used for the parametrization of FG-CNTRC cylindrical curved panels as well as the homogenization approach. Section 3 sets up the basis of the post-buckling analysis of FG-CNTRC cylindrical curved panels. Section 4 presents some comparison analyses with the existing literature as validation study. Afterward, detailed parametric analyses are presented to show the influence of the main micromechanics variables, namely filler content, fiber orientation, fiber distribution, misalignment of fibers, waviness and agglomeration, on post-buckling analysis of FG-CNTRC curved panels under axial compressive forces. Finally, Section 5 presents the conclusions derived from this work.

2. FG-CNTRC curved cylindrical panels

The FG-CNTRC curved cylindrical panels analyzed in this research work are sketched in Fig. 1. The panel is defined by an x-y-z curvilinear coordinate system with the origin at the center of the panel. The x-axis is parallel to the straight edges, the z-axis is directed, outward the surface of the panel, and the y-axis is the circumferential coordinate. Displacements u, v and w refer to the mid-surface axial, circumferential and out-of-plane displacements, respectively. Rotational degrees of freedom noted as ϕ_x and ϕ_y stand for rotations around x- and y-axis, respectively. The axial compression loading condition is defined by an uniformly distributed load N_x along the curved edges. The panel is assumed to be thin and of width b, straight length a, radius R, span angle 2β, and uniform constant thickness t. The rise of the curved edges, h, can be computed by simple trigonometric relations as $h = R(1-\cos\beta)$. The CNTs are assumed to be uniaxially aligned at α degrees with respect to the axial direction

(x-axis). A local orthogonal material coordinate system, $\{0 - x_1 x_2 x_3\}$, is defined at every point on the mid-plane with x_2 tangent to the fibers direction, x_1 on the panel mid-plane, and x_3 normal to the panel. In addition, CNTs are functionally graded across the thickness of the panel by four different distributions, namely UD, FG-V, FG-O and FG-X. UD-CNTRC represents the uniform distribution whilst FG-V, FG-O and FG-X CNTRC are linear distributions of carbon nanotubes along the radial direction. According to these distributions, the CNT volume fraction $V_r(z)$ as a function of $z \in [-t/2, t/2]$, is given by:

$$V_r(z) = V_r^* \qquad \text{(UD CNTRC)} \tag{1a}$$

$$V_r(z) = \frac{4\,|z|}{t} V_r^* \qquad \text{(FG-X CNTRC)} \tag{1b}$$

$$V_r(z) = \left(1 + \frac{2z}{t}\right) V_r^* \qquad \text{(FG-V CNTRC)} \tag{1c}$$

$$V_r(z) = 2\left(1 - \frac{2\,|z|}{t}\right) V_r^* \qquad \text{(FG-O CNTRC)} \tag{1d}$$

being V_r^* the total volume fraction of CNTs.

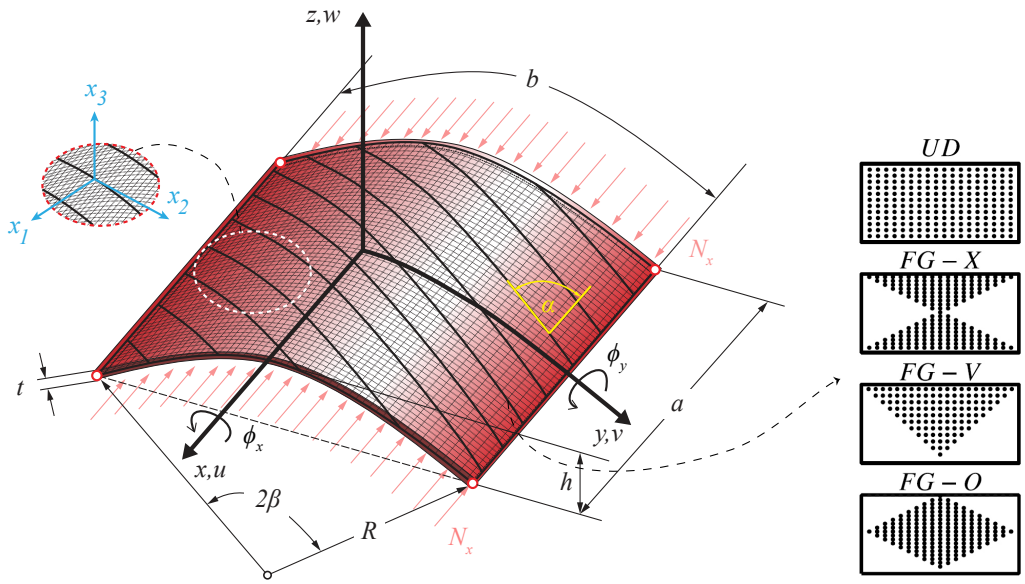

Figure 1: Geometry and coordinate system of FG-CNTRC cylindrical panel.

2.1. Micromechanical modelling of CNTRCs

This subsection introduces the micromechanics framework considered in this research work. The analyses are categorized according to three different configurations, namely polymers doped with straight CNTs, uniaxially aligned curved CNTs, and randomly dispersed fibers with agglomeration effects.

2.1.1. Composites reinforced with straight CNTs.

Consider a linear elastic polymer matrix doped with dispersed long straight CNTs. In order to characterize the effective mechanical properties of the composite, let us now define the Representative Volume Element (RVE) of Fig. 2. It is assumed that the RVE contains a sufficient number of fillers in such a way that the overall properties of the composite are statistically represented [65].

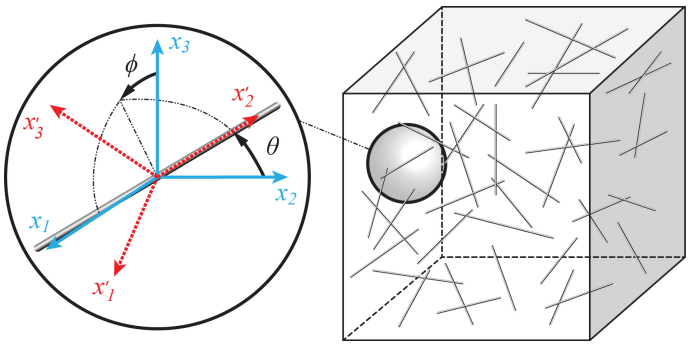

Figure 2: Representative Volume Element (RVE) including straight CNTs.

There exists a variety of methods to estimate the overall properties of composites, among which, the Mori-Tanaka (MT) method [54] is widely used for its simplicity. The MT method extends the theory of Eshelby [66, 67], limited to dilute dispersions of inclusions in an elastic, homogeneous and isotropic medium, to the case of multiple inhomogeneities. First, it is assumed that all the fibers are equal and aligned. Hence, according to Benveniste's revision [68], the effective stiffness of a two-phase composite can be expressed as:

$$\mathbf{C} = (V_m\mathbf{C}_m + V_r\mathbf{C}_r : \mathbf{A}) : (V_m\mathbf{I} + V_r\mathbf{A})^{-1} \tag{2}$$

where, and throughout the paper, a boldface letter stands for a fourth-order tensor, $\mathbf{A} \equiv A_{ijkl}$, and a colon between two tensors denotes inner product, $\mathbf{AB} \equiv A_{ijkl}B_{klmn}$. $\mathbf{C}_m$ is the stiffness tensor of the hosting matrix, $\mathbf{C}_r$ is the stiffness tensor of the equivalent fiber, and $\mathbf{I}$ is the fourth rank identity tensor. V_m denotes volume fraction of the matrix, i.e. $V_m = 1 - V_r$. The tensor $\mathbf{A}$ is the so-called dilute strain concentration tensor and is given by:

$$\mathbf{A} = \left[\mathbf{I} + \mathbf{S} : (\mathbf{C}_m)^{-1} : (\mathbf{C}_r - \mathbf{C}_m)\right]^{-1} \tag{3}$$

with $\mathbf{S}$ being the Eshelby's tensor extensively documented in Eshelby [66] and Mura [69]. The matrix is assumed to be elastic and isotropic with Young's modulus E_m and Poisson's ratio ν_m, or alternatively, shear constant G_m and bulk modulus K_m. Each straight CNT is modeled as an equivalent long fiber with transversely isotropic elastic properties. In this case, assuming that all the fibers are uniaxially aligned in x_2 axis, the composite is also transversely isotropic with a constitutive tensor $\mathbf{C}$ of the form:

$$\mathbf{C} = \begin{bmatrix} k+m & l & k-m & 0 & 0 & 0 \\ l & n & l & 0 & 0 & 0 \\ k-m & l & k+m & 0 & 0 & 0 \\ 0 & 0 & 0 & p & 0 & 0 \\ 0 & 0 & 0 & 0 & m & 0 \\ 0 & 0 & 0 & 0 & 0 & p \end{bmatrix} \tag{4}$$

where k, l, m, n and p are Hill's elastic moduli [70]; k is the plane-strain bulk modulus normal to the fiber direction, n is the uniaxial tension modulus in the fiber direction (x_2), l is the associated cross modulus, m and p are the shear moduli in planes normal and parallel to the fiber direction, respectively.

In order to define more general fiber orientation distributions, such as the one sketched in Fig. 2, the approach proposed by Schjødt-Thomsen and Pyrz [71] is used in this paper. This approach utilizes a direct integration of the stiffness tensor in Eq. (2) weighted by an Orientation Distribution Function (ODF), $\Omega(\phi, \theta)$. To this aim, a local material coordinate system $\left\{0 - x'_1x'_2x'_3\right\}$ is defined to describe the fiber orientation as shown in Fig. 2. The local coordinate system for a radial symmetric inclusion, as it is the case for transversely isotropic cylindrical inclusions, is fully characterized by two Euler angles, ϕ and θ. Hence, the base vectors $\mathbf{e}_i$ and $\mathbf{e}'_i$ of the global, $\left\{0 - x_1x_2x_3\right\}$, and local material coordinate systems, $\left\{0 - x'_1x'_2x'_3\right\}$, are thus related via the transformation matrix $\mathbf{g}$:

$$\mathbf{e}_i = g_{ij}\mathbf{e}'_j \tag{5}$$

where $\mathbf{g}$ is defined by the successive rotations around global x_2 and x_1 axes as:

$$\mathbf{g} = \begin{bmatrix} \cos(\phi) & -\sin(\theta)\sin(\phi) & -\cos(\theta)\sin(\phi) \\ 0 & \cos(\theta) & -\sin(\theta) \\ \sin(\phi) & \cos(\phi)\sin(\theta) & \cos(\theta)\cos(\phi) \end{bmatrix} \tag{6}$$

The stiffness C_{ijlk} in the global material coordinate system is related to the stiffness C'_{pqrs} in the local material coordinate system through the transformation rule of fourth-order tensors:

$$C_{ijlk} = g_{ip}g_{jq}g_{kr}g_{ls}C'_{pqrs} \tag{7}$$

Finally, in order to incorporate the stiffness contribution from all orientations, $\mathbf{C}(\phi, \theta)$ is weighted by the ODF and integrated over all orientations as [71]:

$$\langle \mathbf{C} \rangle = \frac{\int_0^{2\pi} \int_0^{\pi/2} \mathbf{C}(\phi, \theta)\Omega(\phi, \theta) \sin\theta \mathrm{d}\phi \mathrm{d}\theta}{\int_0^{2\pi} \int_0^{\pi/2} \Omega(\phi, \theta) \sin\theta \mathrm{d}\phi \mathrm{d}\theta} \tag{8}$$

2.1.2. Composites reinforced with aligned curved CNTs.

The wavy state of CNTs has been widely reported in the literature [7, 50–53]. Due to their large aspect ratio, with typical lengths between 0.1 and 10 μm and diameters ranging from 10 to 15 nm, as well as very low bending stiffness, CNTs usually present a certain degree of waviness. In the present work, the simulation of the wavy state of CNTs is conducted by means of the helical approach proposed by Shi *et al.* [56]. Fig. 3 shows the parametrization of a helical curved CNT. This three-dimensional curve is defined by its diameter D, the spiral angle θ^w, and the polar angle γ. The length L of the curved CNT is related to these parameters by:

$$L = \frac{\gamma D}{2\cos\theta^w} \tag{9}$$

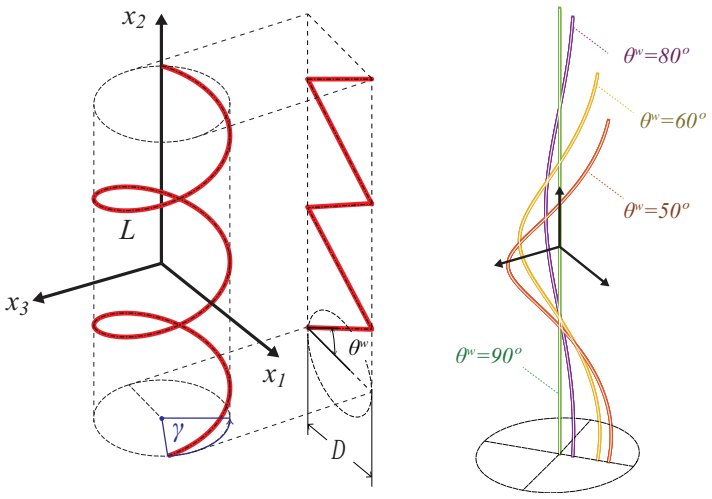

Figure 3: Helical model of a curved CNT.

The waviness of the CNT is governed by the spiral angle, θ^w. For instance, $\theta^w = \pi/2$ corresponds to a straight CNT, while $\theta^w = 0$ corresponds to a circular CNT. Then, under the assumption of a curved CNT composed by a series of successive straight fibers, the tensor of effective elastic moduli of a fully aligned wavy CNTs reinforced composite can be obtained on the basis of the MT method as [56]:

$$\begin{aligned}\mathbf{C} = &\left[\frac{V_r}{\gamma}\int_0^{\gamma}\left(\mathbf{C}_r(\theta^w, s) : \mathbf{A}(\theta^w, s) : \mathbf{C}_m^{-1}\right)\mathrm{d}s + V_m\mathbf{I}\right] : \\ &: \left[\frac{V_r}{\gamma}\int_0^{\gamma}\left(\mathbf{A}(\theta^w, s) : \mathbf{C}_m^{-1}\right)\mathrm{d}s + V_m\mathbf{C}_m^{-1}\right]^{-1}\end{aligned} \tag{10}$$

In this research work, waviness is only taken into consideration for fully aligned filler configurations. As already discussed by Shi *et al.* [56], the theoretical assumption of infinitely long consecutive fiber segments, and thus an Eshelby's tensor corresponding to long rod-like inclusions, yields the same results for both randomly dispersed wavy and straight CNTs.

2.1.3. Agglomeration of CNTs.

A second important phenomenon to be taken into consideration for the simulation of CNT nano-reinforced composites is the appearance of non-uniform spatial distributions of inclusions. The difficulty in obtaining good fiber dispersions is related to the circumstance that CNTs tend to agglomerate in bundles. As previously introduced, this effect is attributed to the electronic configuration of tube walls and their high specific surface area which increases the van der Waals (vdW) attraction forces among nanotubes [48, 49, 72]. It is reported extensively in the literature that bundles can substantially decrease the overall mechanical properties of the composites. As a result, a rigorous modeling of CNT reinforced composites must consider the presence of clustering of CNTs in bundles. In this paper, the two-parameter agglomeration model introduced by Shi *et al*. [56] is adopted. Hence, the total volume V_r of CNTs in the volume V of the RVE is divided into the following two parts:

$$V_r = V_r^{bundles} + V_r^m \tag{11}$$

where $V_r^{bundles}$ and V_r^m denote the volumes of CNTs dispersed in the bundles and in the matrix, respectively. In order to characterize the agglomeration of CNTs in bundles, two parameters ξ and ζ are introduced as follows:

$$\xi = \frac{V_{bundles}}{V}, \quad \zeta = \frac{V_r^{bundles}}{V_r} \tag{12}$$

where $V_{bundles}$ is the volume of the bundles in the RVE, and ξ denotes the volume fraction of the bundles with respect to the total volume V of the RVE. When ξ=1, nanotubes are uniformly dispersed in the matrix, and with the decrease in ξ, the agglomeration degree of CNTs is more severe. The parameter ζ denotes the volume ratio of nanotubes that are dispersed in bundles and the total volume of nanotubes. When ζ=1, all the nanotubes are located in the bundles. In the case where all nanotubes are uniformly dispersed, one has that ξ=ζ. The bigger the value ζ with $\zeta > \xi$, the more heterogeneous the spatial distribution of CNTs (see Fig. 4). On this basis, the previously presented micromechanics model can be extended to the case of non-uniform distributions by considering bundles as sphere inclusions. In the case of randomly oriented CNTs, the effective bulk moduli K_{in} and K_{out} and the effective shear moduli G_{in} and G_{out} of the bundles and the matrix are given, respectively by [56]:

$$K_{in} = K_m + V_r \frac{(\delta_r - 3K_m\alpha_r)\zeta}{3(\xi - V_r\zeta + V_r\zeta\alpha_r)} \tag{13a}$$

$$K_{out} = K_m + V_r \frac{(\delta_r - 3K_m\alpha_r)(1-\zeta)}{3\left[1 - \xi - V_r(1-\zeta) + V_r(1-\zeta)\alpha_r\right]} \tag{13b}$$

$$G_{in} = G_m + V_r \frac{(\eta_r - 2G_m\beta_r)\zeta}{3(\xi - V_r\zeta + V_r\zeta\beta_r)} \tag{13c}$$

$$G_{out} = G_m + V_r \frac{(\eta_r - 2G_m\beta_r)(1-\zeta)}{2\left[1 - \xi - V_r(1-\zeta) + V_r(1-\zeta)\beta_r\right]} \tag{13d}$$

with

$$\alpha_r = \frac{3\left(K_m + G_m\right) + k_r - l_r}{3\left(G_m + k_r\right)} \tag{14a}$$

$$\beta_r = \frac{1}{5}\left\{\frac{4G_m + 2k_r + l_r}{3\left(G_m + k_r\right)} + \frac{4G_m}{G_m + p_r} + \frac{2\left[G_m\left(3K_m + G_m\right) + G_m\left(3K_m + 7G_m\right)\right]}{G_m\left(3K_m + G_m\right) + m_r\left(3K_m + 7G_m\right)}\right\} \tag{14b}$$

$$\delta_r = \frac{1}{3}\left[n_r + 2l_r + \frac{\left(2k_r + l_r\right)\left(3K_m + 2G_m - l_r\right)}{G_m + k_r}\right] \tag{14c}$$

$$\eta_r = \frac{1}{5}\left[\frac{2}{3}\left(n_r - l_r\right) + \frac{8m_rG_m\left(3K_m + 4G_m\right)}{3K_m\left(m_r + G_m\right) + G_m\left(7m_r + G_m\right)} + \frac{8G_mp_r}{G_m + p_r} + \frac{2\left(k_r - l_r\right)\left(2G_m + l_r\right)}{3\left(G_m + k_r\right)}\right] \tag{14d}$$

The Eshelby's tensor for spherical inclusions reads [69]:

$$S_{1111} = S_{2222} = S_{3333} = \frac{7 - 5\nu_{out}}{15(1 - \nu_{out})} \tag{15a}$$

$$S_{1122} = S_{2233} = S_{3311} = -\frac{1 - 5\nu_{out}}{15(1 - \nu_{out})} \tag{15b}$$

$$S_{1212} = S_{2323} = S_{3131} = \frac{4 - 5\nu_{out}}{15(1 - \nu_{out})} \tag{15c}$$

where $\nu_{out} = (3K_{out} - 2G_{out})/2(3K_{out} + G_{out})$ is the Poisson's ratio of the hybrid matrix, i.e. matrix doped with low filler content surrounding the bundles. Finally, the overall bulk modulus, K, and the effective shear modulus, G, of the composite are derived from the MT method as:

$$K = K_{out}\left[1 + \frac{\zeta\left(\frac{K_{in}}{K_{out}} - 1\right)}{1 + \alpha_K(1 - \xi)\left(\frac{K_{in}}{K_{out}} - 1\right)}\right] \tag{16a}$$

$$G = G_{out}\left[1 + \frac{\zeta\left(\frac{G_{in}}{G_{out}} - 1\right)}{1 + \beta_K(1 - \xi)\left(\frac{G_{in}}{G_{out}} - 1\right)}\right] \tag{16b}$$

with $\alpha_K = (1 + \nu_{out})/3(1 - \nu_{out})$ and $\beta_K = 2(4 - 5\nu_{out})/15(1 - \nu_{out})$.

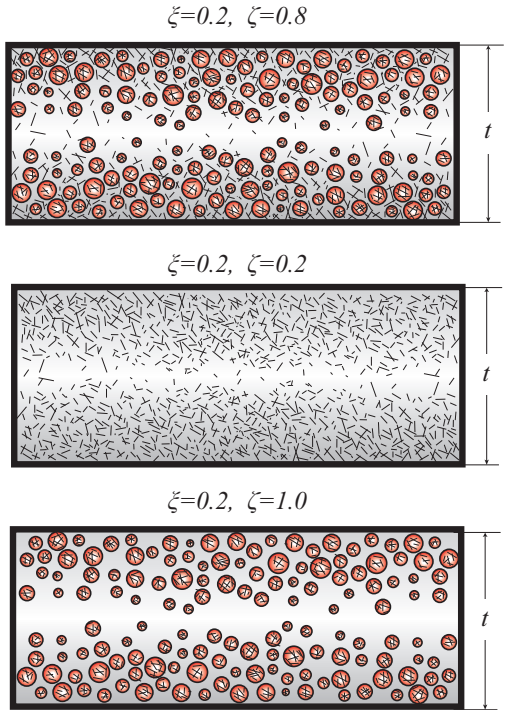

Figure 4: Schematic illustration of the variation of the parameters ξ and ζ of the two-parameter agglomeration model for a FG-X filler distribution.

3. Numerical solution

The numerical studies are conducted with the commercial Finite Element (FE) code ANSYS. Panels are modeled with the standard structural shell element, Shell 181 [73], suitable for thin to moderately-thick shell structures. This element type is a quadrilateral 4-nodes element involving both bending and membrane properties with three rotational and three translational degrees of freedom per node. The conventional Newton-Raphson method fails to predict buckling behavior because of the singularity of the stiffness matrix and a diverging solution. Therefore, the arc-length method, suitable for obtaining non-linear static solutions with complex buckling behaviors such as secondary buckling, snap-back, or snap-through, has been used in this study. In this context, the load-displacement path is traced by the equilibrium states of the structure subjected to increasing load levels. Let us define the equilibrium configuration at instant t_i by the pair:

$$\left\{\lambda_i \bar{\mathbf{f}}^e, \mathbf{u}_i\right\} \tag{17}$$

where the system is defined by the vector of external nodal forces, $\lambda_n \bar{\mathbf{f}}^e$, and nodal displacements, $\mathbf{u}_i$. The parameter λ_i is the load factor that modulates the given external force vector $\bar{\mathbf{f}}^e$. A new equilibrium configuration at an instant, t_{i+1}, is typically obtained by incrementing the load factor with a prescribed incremental load factor, $\Delta\lambda$, as $\lambda_{i+1} = \lambda_i + \Delta\lambda$. Thereupon, the new nodal displacement vector, $\mathbf{u}_{i+1}$, at the new equilibrium state is achieved by minimizing the non-linear residual equation:

$$\mathbf{r}\left(\mathbf{u}_{i+1}, \Delta\lambda\right) \equiv \mathbf{f}^{\,\mathrm{int}}\left(\mathbf{u}_{i+1}\right) - \left(\lambda_i + \Delta\lambda\right)\bar{\mathbf{f}}^e = \mathbf{0} \tag{18}$$

where $\mathbf{r}$ stands for the out-of-balance force vector and $\mathbf{f}^{\,\mathrm{int}}$ denotes the internal load vector. If the Newton-Raphson method is adopted to solve the residual equation, at a typical iteration $k+1$, the new guess, $\mathbf{u}_{i+1}^{(k+1)}$, is obtained as:

$$\mathbf{u}_{i+1}^{(k+1)} = \mathbf{u}_i + \Delta\mathbf{u}^{(k+1)} \tag{19a}$$

$$\Delta\mathbf{u}^{(k+1)} = \Delta\mathbf{u}^{(k)} + \delta\mathbf{u} \tag{19b}$$

with $\Delta\mathbf{u}^{(k)}$ and $\Delta\mathbf{u}^{(k+1)}$ being the incremental displacement guesses for the previous and current iterations, respectively. The iterative displacement, $\delta\mathbf{u}$, is the solution to the linearized residual equation:

$$\mathbf{K}\left(\mathbf{u}_{i+1}^{(k)}\right)\delta\mathbf{u} = -\mathbf{r}\left(\mathbf{u}_{i+1}^{(k)}, \Delta\lambda\right) \tag{20}$$

where $\mathbf{K}$ denotes the standard tangent stiffness matrix.

The arc-length method consists of adding an extra constraint to the residual equation so as to limit the length of the incremental solution. In particular, the spherical arc-length method is aimed to find the intersection of Eq. (18) with a constant term l, so-called arc-length, leading to:

$$\Delta\mathbf{u}^T\Delta\mathbf{u} + \Delta\lambda^2\psi^2\bar{\mathbf{f}}^{eT}\bar{\mathbf{f}}^e - l^2 = 0 \tag{21}$$

with ψ being a scaling parameter for loading terms. Hence, the iterative solution of the non-linear system is derived by simply linearizing the residual equation together with the arc-length constraint:

$$\begin{bmatrix}\mathbf{K}\left(\mathbf{u}^{(k)}\right) & -\bar{\mathbf{f}}^e \\ 2\Delta\mathbf{u}^{(k)T} & 2\Delta\lambda^{(k)}\psi^2\bar{\mathbf{f}}^{eT}\bar{\mathbf{f}}^e\end{bmatrix}\cdot\begin{Bmatrix}\delta\mathbf{u}\\ \delta\lambda\end{Bmatrix} = -\begin{Bmatrix}\mathbf{r}\left(\mathbf{u}^{(k)}, \Delta\lambda^{(k)}\right)\\ \Delta\mathbf{u}^{(k)T}\Delta\mathbf{u}^{(k)} + \left(\Delta\lambda^{(k)}\right)^2\psi^2\bar{\mathbf{f}}^{eT}\bar{\mathbf{f}}^e - l^2\end{Bmatrix} \tag{22}$$

where the subscripts $i+1$ have been omitted for notational convenience. The iterative load factor, $\delta\lambda$, is derived by the general arc-length procedure based on orthogonality principles proposed by Forde and Stiemer [74]. In that work, the authors suggested the selection of an arbitrary direction $\mathbf{n}^{(k)}$ with reference to the tangent $\mathbf{t}^{(k)}$ of the current incremental load-displacement configuration. The tangential and normal vectors consist of m dimensions from the displacement vector and one dimension from the load parameters. These components are combined with the scaling factor η to form vectors with $m+1$ dimension as follows:

$$\mathbf{t}^{(k)} = \mathbf{u}^{(k)} + \eta\lambda^{(k)} \tag{23a}$$

$$\mathbf{n}^{(k)} = \delta\mathbf{u} + \eta\delta\lambda \tag{23b}$$

Rearranging the incremental displacement into two components, $\delta\mathbf{u}^I = -\mathbf{K}^{-1}\mathbf{r}$ and $\delta\mathbf{u}^{II} = \mathbf{K}^{-1}\bar{\mathbf{f}}^e$, as $\delta\mathbf{u} = \delta\mathbf{u}^I + \delta\lambda\delta\mathbf{u}^{II}$, the general expression for $\delta\lambda$ writes:

$$\delta\lambda = \frac{\mathbf{g}^{(k)} + \mathbf{u}^{(k)T}\delta\mathbf{u}^I}{\eta^2\lambda^{(k)} + \mathbf{u}^{(k)T}\delta\mathbf{u}^{II}} \tag{24}$$

where $g^{(k)}$ stands for the residual of the scalar product of $\mathbf{t}^{(k)}$ and $\mathbf{n}^{(k)}$. In particular, for explicit iteration on a sphere this term reads:

$$g^{(k)} = -\frac{l^2}{\left|\mathbf{t}^{(k+1)}\right|}\left(\left|\mathbf{t}^{(k+1)}\right| - l\right) \tag{25}$$

with $\left|\mathbf{t}^{(k+1)}\right|$ being the length of the tangent in the potential configuration:

$$\left|\mathbf{t}^{(k+1)}\right| = \sqrt{\left|\mathbf{t}^{(k)}\right|^2 + \delta\mathbf{u}^T\delta\mathbf{u} + \eta^2\delta\lambda^2} \tag{26}$$

In order to implement the constitutive equations of the resulting CNTRCs into the modeling, the preintegrated general shell sections module of ANSYS is employed. This module allows one to explicitly define the membrane, bending and coupling stiffness matrices of the shells. For this purpose, let us note the constitutive equations of the CNTRCs written in Voigt's notation as follows:

$$\begin{bmatrix}\sigma_{11}\\ \sigma_{22}\\ \sigma_{12}\\ \sigma_{23}\\ \sigma_{13}\end{bmatrix} = \begin{bmatrix}Q_{11}(z) & Q_{12}(z) & 0 & 0 & 0\\ Q_{12}(z) & Q_{22}(z) & 0 & 0 & 0\\ 0 & 0 & Q_{66}(z) & 0 & 0\\ 0 & 0 & 0 & Q_{44}(z) & 0\\ 0 & 0 & 0 & 0 & Q_{55}(z)\end{bmatrix} \cdot \begin{bmatrix}\varepsilon_{11}\\ \varepsilon_{22}\\ \varepsilon_{12}\\ \varepsilon_{23}\\ \varepsilon_{13}\end{bmatrix} \tag{27}$$

$$\begin{array}{lll} Q_{11} = \frac{E_{11}}{1-\nu_{12}\nu_{21}}, & Q_{22} = \frac{E_{22}}{1-\nu_{12}\nu_{21}}, & Q_{12} = \frac{\nu_{21}E_{11}}{1-\nu_{12}\nu_{21}},\\ Q_{66} = G_{12}, & Q_{44} = G_{23}, & Q_{55} = G_{13}\end{array} \tag{28}$$

where E_{11} and E_{22} are effective Young's moduli of CNTRC panels in the local coordinates; G_{12}, G_{13} and G_{23} are the shear moduli; ν_{12} and ν_{12} are Poisson's ratios obtained by the micromechanics homogenization approach. Note that Q_{ij} varies with z according to the grading profile of the fillers across the thickness. Thus, the components of the extensional stiffness, C_E, bending-extension-coupling stiffness, C_C, bending stiffness, C_B, and transverse shear stiffness, C_S, are defined by the following integrals:

$$\begin{array}{l}(C_E^{ij}, C_C^{ij}, C_B^{ij}) = \int_{-t/2}^{t/2} Q_{ij}(z)\cdot(1, z, z^2)\mathrm{d}z \quad (i, j = 1, 2, 6),\\ C_S^{ij} = \frac{1}{ks}\int_{-t/2}^{t/2} Q_{ij}(z)\mathrm{d}z \quad (i, j = 4, 5)\end{array} \tag{29}$$

where ks denotes the transverse shear correction factor for two-phase FGMs, given by Efraim and Eisenberg [75] as:

$$ks = \frac{6 - (\nu_{12}^{CNT}V_r + \nu^m V_m)}{5} \tag{30}$$

4. Results and discussion

In this section, several numerical examples are presented to study the post-buckling behavior of FG-CNTRC curved panels under uniform axial compression. Poly (methyl methacrylate) (PMMA) is selected as the matrix material with Young's modulus E_m=2.5 GPa and Poisson's ratio ν_m=0.34 with a room temperature of T=300 K. Armchair (10,10) SWCNTs are selected as reinforcements. The Hill's moduli of the CNTs are extracted from the analytical results of Popov et al. [76] as k_r=30 GPa, l_r=10 GPa, $m_r = p_r$=1 GPa and n_r=450 GPa. For the subsequent analyses, the geometrical properties $a = b$ = 0.2 m, t =a/50, and h =0.025b are set up, unless otherwise indicated. In order to evaluate the imperfection sensitivity of the panels, a small initial imperfection, $w_0 = 0.1t$, is also considered in the transverse direction following the first buckling mode. Two types of boundary conditions are considered in the numerical analyses: clamped curved edges and simply supported straight edges (CSCS), and four edges simply supported (SSSS). The restrictions of the considered boundary conditions are summarized in Table 1. The compressive load is introduced by applying the uniform axial load N_x to the Edge 1 at x=-a/2.

Table 1: Boundary conditions for the post-buckling analysis of curved panels under axial compression

	SSSS					CSCS				
	u	v	w	ϕ_x	ϕ_y	u	v	w	ϕ_x	ϕ_y
Corner 1 (x=-a/2,y=b/2)	cpl	0	1	1	1	cpl	0	1	1	1
Corner 2 (x=-a/2,y=-b/2)	cpl	0	1	1	1	cpl	0	1	1	1
Corner 3 (x=a/2,y=-b/2)	1	0	1	1	1	1	0	1	1	1
Corner 4 (x=a/2,y=b/2)	1	1	1	1	1	1	1	1	1	1
Edge 1 (x=-a/2)	cpl	0	1	1	0	cpl	0	1	1	1
Edge 2 (y=-b/2)	0	0	1	0	1	0	0	1	0	1
Edge 3 (x=a/2)	1	0	1	1	0	1	0	1	1	1
Edge 4 (y=b/2)	0	0	1	0	1	0	0	1	0	1

(cpl coupled; 1 restrained; 0 free).

The numerical results are divided into comparison and validation studies, and parametric analyses. The aim of the first set of tests is the validation of the proposed approach. In particular, post-buckling analyses of isotropic flat and curved panels have been compared to benchmark solutions in the literature. In addition, results of FG-CNTRC flat and curved panels have been also compared to previously published results.

4.1. Comparison studies

In this subsection, post-buckling analyses of isotropic aluminum flat and cylindrical panels are considered first to validate the present approach. In addition, comparison analyses of non-linear buckling response of FG-CNTRC flat and cylindrical panels are also presented.

4.1.1. Isotropic flat panels

To verify the present approach, an isotropic square plate subjected to edge compression is considered first. In particular, the analytical and experimental results by Yamaki [77, 78] are taken as validation benchmark. The length-to-thickness ratio is a/t=120, and the Poisson's ratio is ν=1/3. A non-dimensional load factor N_b is defined as $N_b = Na^2/\pi^2 Et^3$, with E being the Young's modulus of the plate. Fig. 5 shows the variation of the non-dimensional load factor N_b against the non-dimensional central displacement w/h. Two different imperfection values have been used according to [77], namely $w_0 = 0$ and $w_0 = 0.1t$. Two different boundary conditions have been considered, Fig. 5(a) with all the edges simply supported, and the unloaded edges free to move laterally along the plane of the plate (SSSS), and 5(b), considering that the loaded edges are clamped, and the unloaded edges are simply supported (CSCS). It can be seen that the present approach provides very close results to the analytical solution of Yamaki [77] for both boundary conditions. The experimental results are also very close to the theoretical solutions in the case of SSSS boundary conditions. Nonetheless, larger differences can be observed in the case of CSCS boundary conditions in the post-buckling stage in Fig 5(a). These differences with the experimental data are justified in the same manner as in [78], where Yamaki hypothesized that the condition of free rotation along the loaded edges was not fully satisfied by the experimental fixture.

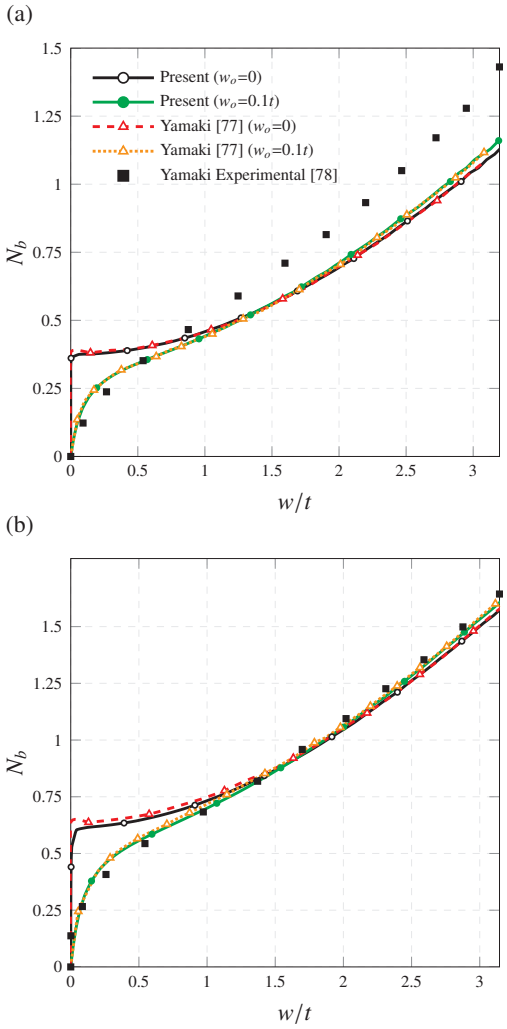

Figure 5: Comparison analysis of the post-buckling response of a simply supported (SSSS) (a), and simply supported with loaded edges clamped (CSCS) isotropic square plate (b) (a=b, a/t=120, h = 0, ν=1/3).

4.1.2. Isotropic curved panels

Secondly, the post-buckling behavior of an isotropic aluminum cylindrical panel studied by Thornburgh and Hilburger [18] and Liew *et al*. [79] is analyzed. The material and geometric properties of this aluminum cylindrical panels are Young's modulus E=68947.45 MPa, Poisson ratio ν=0.33, length a=37.47 cm, width b=36.83 cm, nominal thickness t=3.30 mm, and radius R=1.52 m. The results reported by Thornburgh and Hilburger [18] were obtained by using a finite element method based on Kirchoff-Love thin shell theory, while Liew *et al*. [79] used a meshless Ritz method. Fig. 6(a) shows the central deflection w of the panel subjected to axial compression load P_b=$N_x b$. The corresponding end-shortening response is shown in Fig. 6(b). It can be seen that very close results are obtained in the pre-buckling and mid- stages in comparison to Thornburgh and Hilburger's results. A reasonable agreement can be observed in the post-buckling stage although, since different shell theories are adopted, larger differences are found. A similar reasoning can be applied to the comparison against the results reported by Liew *et al*. In this case, Liew and co-authors presented closer results to Thornburgh and Hilburger's ones in the post-buckling stage. However, larger differences are observed in the linear pre-buckling stage.

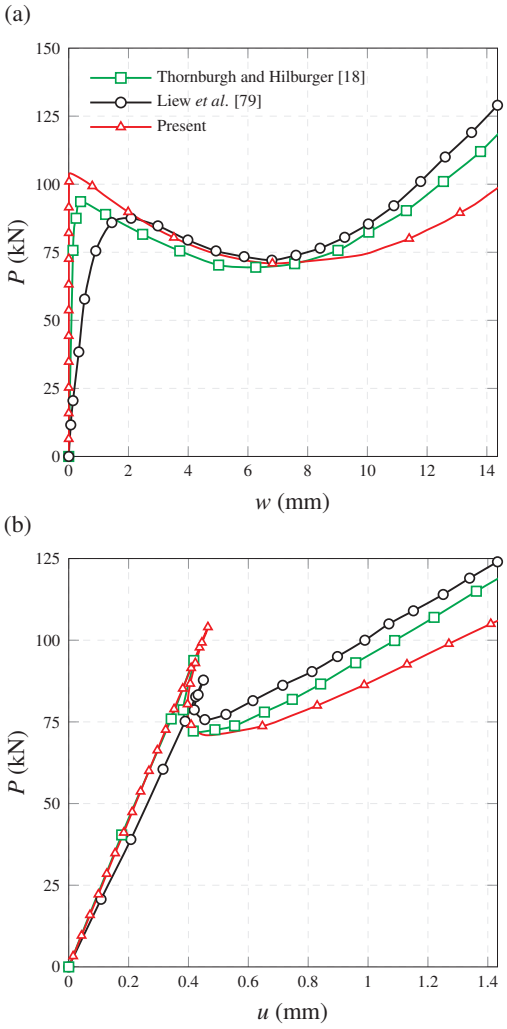

Figure 6: Central deflection (a), and end shortening (b) of a curved isotropic aluminum panel under axial compression with CSCS boundary conditions (E=68947.45 MPa, ν=0.33, a=37.47 cm, b=36.83 cm, t=3.30 mm, R=1.52 m).

4.1.3. FG-CNTRC flat and curved panels

Finally, the present approach is compared to existing literature results on the post-buckling response of FG-CNTRC flat and curved panels. The element-free ILMS-Ritz results reported by Zhang *et al.* [40] and Liew *et al.* [79] are taken as validating benchmarks for flat and cylindrical curved panels, respectively. In both cases, PMMA is selected as matrix material and (10,10) SWCNTs as reinforcements. A small initial imperfection of value $w_0 = 0.1t$ is also considered in the transverse direction according to the first buckling mode. A volume fraction of V_c^*=0.12 and CSCS boundary conditions are chosen for comparison. The authors [40, 79] considered slightly different boundary conditions as those in Table 1. In particular, the compressive load was applied to both curved edges and no restrictions were defined for the axial displacements u. For comparison purposes, those boundary conditions are also used in this analysis. Reinforcement grading profiles type UD, FG-O and FG-X are compared. It is important to note that in both references [40] and [79], the effective properties of the FG-CNTRCs were computed by the extended rule of mixtures [80, 81]. It has been extensively discussed in the literature the synergism between the Eshelby-Mori-Tanaka model and the Extended Rule of Mixtures (EROM) in the case of uniaxially aligned CNT reinforced composites [82], as well as in our previous work [64] were both approaches were compared for the linear buckling analysis of FG-CNTRC curved panels with excellent correlations. In this comparison analysis, the EROM is also used with efficiency parameters η_1=0.137, η_2=1.022, η_3=0.715. For paucity of space, the formulation of the EROM is here omitted so readers are invited to consult [64] (c.f. [40, 42, 79]).

Firstly, the central deflection and end-shortening of FG-CNTRC flat panels are shown in Figs. 7(a) and (b), respectively. The geometrical properties of the flat panel are a=b=1 m and t/a=0.01. Secondly, the results for the central deflection and end-shortening of FG-CNTRC curved panels are shown in Figs. 7(c) and (d), respectively. In this case, the geometrical properties are $a = b$ =0.2 m, R=1 m and t=0.004 m. It can be observed that very

close results were obtained for both flat and curved configurations. In view of these results, along with the previous analyses, it can be concluded that the proposed approach is accurate for the post-buckling analysis of FG-CNTRC curved panels.

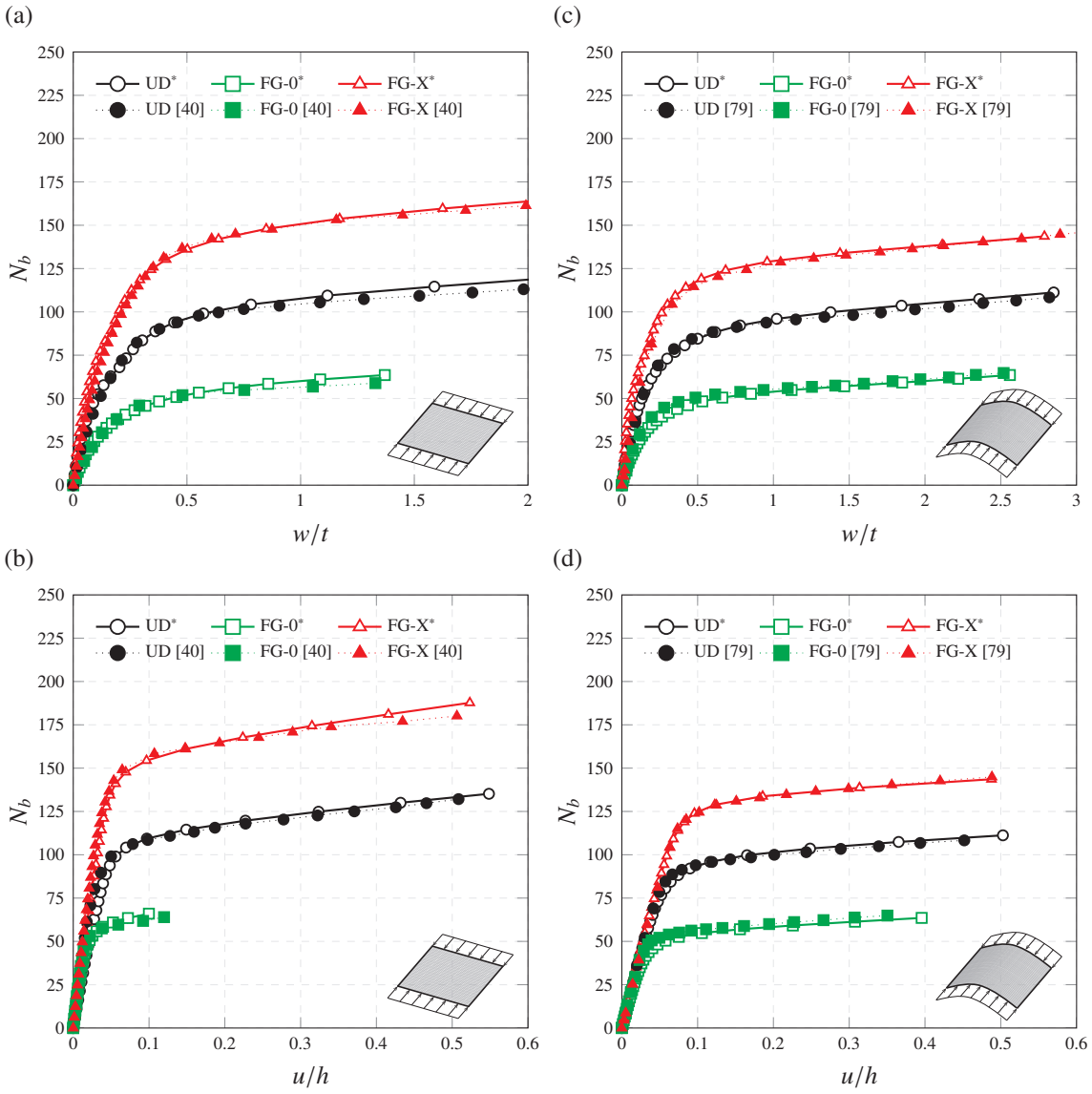

Figure 7: Non dimensional central deflection and end-shortening of FG-CNTRC flat (a)-(b) and curved panels (c)-(d) with CSCS boundary conditions ((10,10) SWCNT/PMMA, V_c^*=0.12, α = 0, $w_0 = 0.1t$; flat panels: a=b=1 m and t/a=0.01; curved panels: a = b =0.2 m, R=1 m and t=0.004 m).

4.2. Parametric analyses

In this section, parametric studies concerning the effect of CNTs volume fraction, fibers angle, reinforcements distribution, orientation distribution of CNTs, waviness and agglomeration, are presented. The purpose of these analyses is to investigate the effect of these micromechanical variables on the post-buckling response of FG-CNTRCs, as well as to extract conclusions for the manufacturing of high-performance FG-CNTRC curved panels under axial compression conditions. For completeness of the results, the analyses with an initial geometrical imperfection $w_0 = 0.1t$ are also included, corresponding to dotted curves in all the subsequent results.

4.2.1. Effect of volume fraction of CNTs

Firstly, the post-buckling paths of FG-CNTRC curved panels are analyzed for different filler contents. In particular, CNT volume fractions of 0, 1, 5 and 10% are selected as shown in Fig. 8. Uniform (UD) distributions of nanotubes are considered as well as CSCS boundary conditions. Figs. 8(a) and (b) show the non-dimensional

central deflection and end-shortening, respectively. We first note that the limit points and the subsequent snap-through buckling paths, as in the case of neat polymer V_r=0%, tend to disappear as the filler content grows. In these cases, as for instance a filler content of V_r=10%, the central deflection increases slowly in the pre-buckling stage and increases very fast in the post-buckling stage. In addition, the relationship between the end-shortening and the load parameter is almost bi-linear. As expected, higher SWCNT contents lead to stiffer panels and, therefore, higher critical buckling loads. For example, a filler content of 5% yields an increase of the critical buckling load of five times that of the neat polymer, V_r=0%. The increases in the bending stiffness of the panels can be clearly seen in Fig. 8(a) where, in the post-buckling stage, the slope of the equilibrium path increases admitting higher load levels. In terms of axial stiffness, similar conclusions can be extracted from Fig. 8(b).

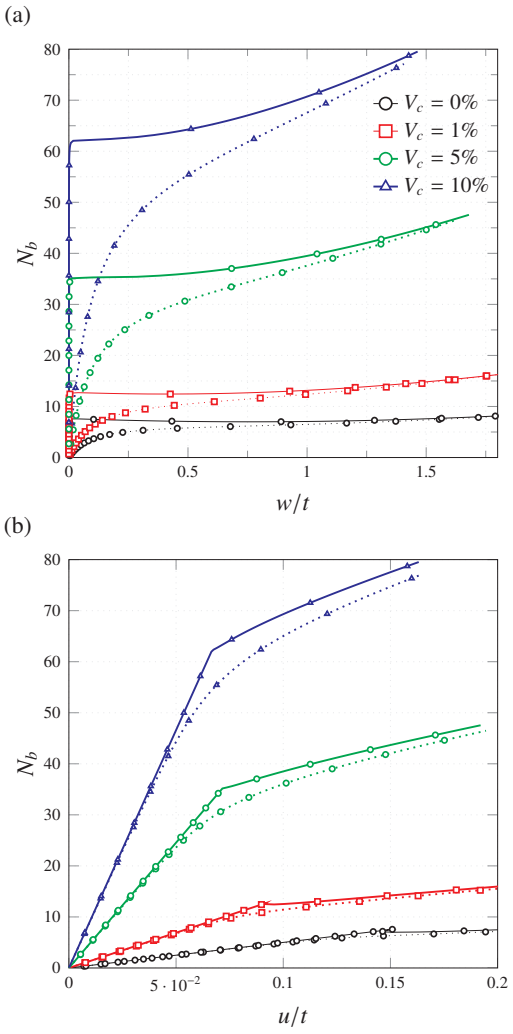

Figure 8: Non-dimensional central deflection (a) and end-shortening (b) of uniaxially compressed FG-CNTRC curved panels with CSCS boundary conditions and different SWCNT contents (UD, a=b=1 m, t =a/50 , h =0.025b, α = 0). Solid and dotted lines denote the results for perfect and imperfect (w_0 = 0.1t) panels, respectively.

4.2.2. Effect of CNTs orientation

In this set of analyses, the effect of the fibers orientation, denoted by angle α, is investigated. CNTs exhibit a high level of anisotropy, with transverse elastic modulus on average two orders of magnitude higher than the transverse modulus. This fact suggests the importance of conveniently define the orientation of the fillers to maximize the mechanical response of the composites. In order to highlight this issue, Fig. 9 shows the post-buckling paths of UD-CNTRC flat panels, (a) and (b), and curved panels, (c) and (d), for various fiber angles α. In particular, angles of 0°, 20°, 40°, 60° and 90° have been selected. For the sake of clarity in the results, the panels have been defined with geometrical properties b = 0.2 m, a = 2b, t =a/50, as well as h = 0 and h = 0.025b for flat and curved panels, respectively. Uniform (UD) CNTs distributions with V_c = 0.12 and SSSS boundary conditions have been considered. In accordance with our previous work [64], CNTs orientation has a crucial effect on the critical buckling loads as clearly displayed in Fig. 9. In addition, it was shown in that work that curvature

raises the critical buckling loads, as also reflected here when comparing Figs. 9(a) and (c). In the case of flat panels with aspect ratio a/b=2, our previous work also reported that the critical buckling loads reach maximum values around 45°. Accordingly, it can be seen in Fig. 9(a) that the maximum load values are those for fiber angles 40° and 60°, whilst fiber angles 0° and 90° yield very similar results. However, the slopes of the post-buckling paths are maximum for the latter cases. This fact is also evident in the end-shortening results in Fig. 9(b). The largest axial stiffness corresponds to the fibers angle $\alpha = 0°$, case in which CNTs are aligned in the direction of the axial loading. With regard to curved FG-CNTRC panels, the behavior is fairly different as expected from our previous work [64]. In this case, as curvature increases, the maximum buckling loads tend to shift towards $\alpha = 0°$, even appearing minimum buckling loads for fiber angles above 45°. It can be seen in Fig. 9(c) that the maximum buckling load appears for $\alpha = 40°$, while the case of $\alpha = 60°$ has a buckling load under the one with $\alpha = 20°$, which is in accord with the previously discussed behavior. We also find that, unlike the flat configuration, there is a limit point and an unstable region before the post-buckling stage for some fibers angles such as 20° and 40°. Finally, the deformed shapes of the panels have been also included in Fig. 9. As expected, the fibers orientation has a critical influence on the buckling modes and, therefore, on the post-buckling equilibrium configurations.

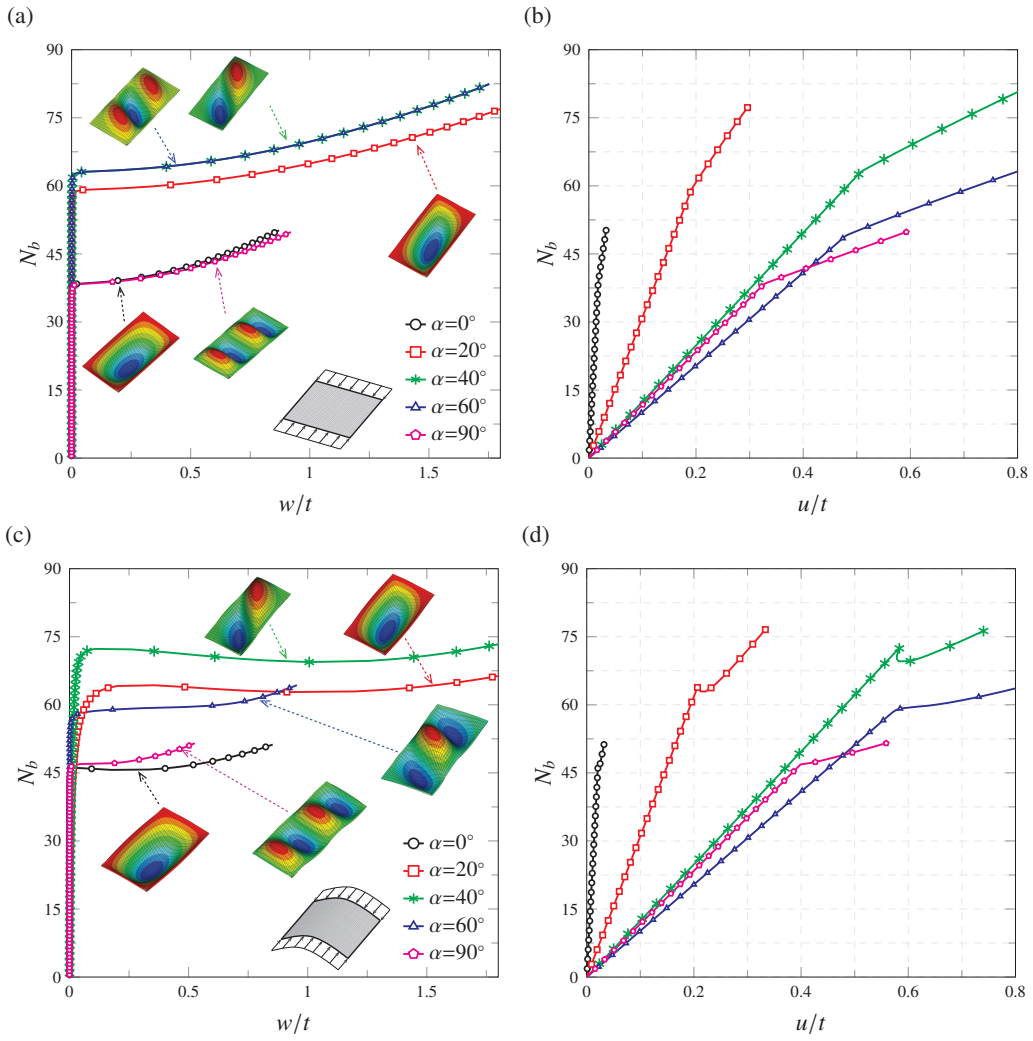

Figure 9: Post-buckling path of FG-CNTRC flat, (a) and (b), and curved panels, (c) and (d), with SSSS boundary conditions and different SWCNT fiber angles α (UD, a=b=1 m, t =a/50 , h =0.025b, V_c = 0.12).

4.2.3. Effect of CNTs distribution

The post-buckling behavior of FG-CNTRC curved panels with different CNTs distributions, namely UD, FG-V, FG-O, and FG-X, is studied for CSCS and SSSS boundary conditions in Figs. 10(a) and (b), and (c) and (d), respectively. First of all, let us focus on the V type distribution. It can be seen in Fig. 10(c) that the FG-V distribution does not exhibit a critical buckling load and presents an unstable response (the analysis with initial imperfection has been omitted for clarity). As already discussed by other authors [29, 30], this behavior is explained by the coupling between membrane and bending stiffnesses induced by the asymmetry of the distribu-

tion. Conversely, this coupling is lost in the case of CSCS boundary condition as shown in Fig. 10(a). In this case, the rotational restraint deletes the bending-extension coupling and the panels thus exhibit typical pre- and post-buckling behaviors. With respect to the rest of distributions, it can be seen that FG-O leads to the lowest post-buckling strength, while FG-X yields the highest post-buckling strength among the four types of distributions for both boundary conditions. In the case of CSCS boundary condition, where FG-V does originate initially stable panels, CNTs distributed according to FG-V profile yields post-buckling paths between those by UD and FG-O. It can be therefore concluded that CNTs distributed close to the top and bottom surfaces increase more efficiently the stiffness and post-buckling strength of the FG-CNTRC cylindrical panels than CNTs distributed near the mid-plane.

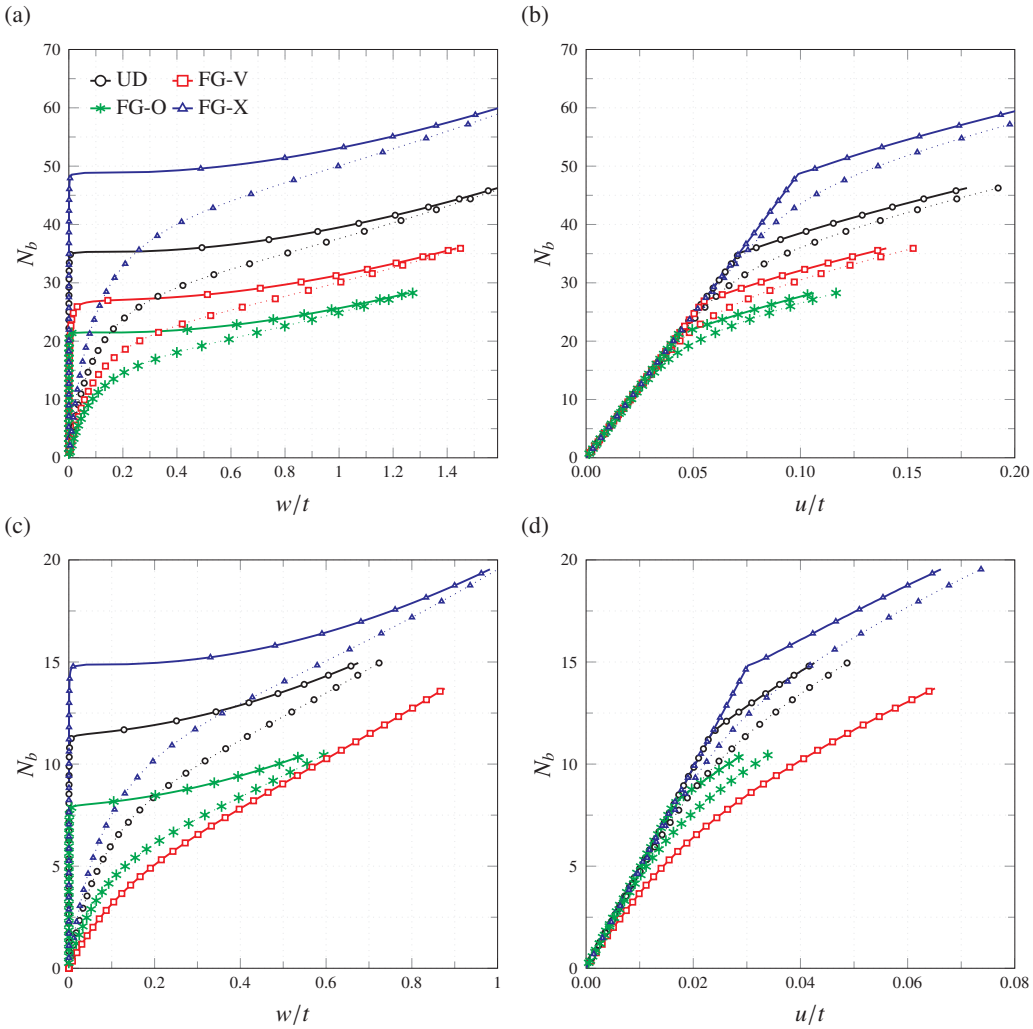

Figure 10: Post-buckling path of FG-CNTRC curved panels with CSCS, (a) and (b), and SSSS, (c) and (d), boundary conditions and different SWCNTs distributions (a=b=1 m, t =a/50 , h =0.025b, V_c = 0.12, α = 0). Solid and dotted lines denote the results for perfect and imperfect (w_0 = 0.1t) panels, respectively.

4.2.4. Effect of orientation distribution of CNTs

In this series of analyses, the influence of CNTs misalignment on the post-buckling behavior of UD-CNTRC curved panels is investigated. To this aim, the orientation distribution function in Eq. (8) is here defined as a symmetric truncated normal distribution. This type of distribution is said to have azimuthal symmetric and, thus, only one Euler angle is needed for its definition. Hence, the orientation distribution function, $\Omega(\theta)$, is defined as a truncated Gaussian distribution with mean value $\theta = 0^\circ$, and θ ranging from $-\pi/2$ to $\pi/2$, with standard deviation σ. Fig. 11 shows the resulting ODFs with different standard deviations. Any general orientation distribution is comprised between the limit cases of fully aligned, $\sigma = 0^\circ$, and randomly oriented fillers, $\Omega(\theta) = 1$. In the case of fully aligned, the overall composites are transversely isotropic, whilst randomly oriented CNTs yield isotropic composites. Thence, the degree of anisotropy depends upon the alignment of the fillers.

On this basis, Fig. 12 shows the post-buckling behavior of UD-CNTRC curved panels with different degrees

of CNTs misalignment. It is observed that misalignment of fillers has a substantial effect on the critical buckling loads. The highest critical buckling loads are obtained for fully aligned SWCNTs configurations, i.e. $\sigma = 0°$, and decrease with the misalignment degree, i.e. with decreasing standard deviation values. In addition, not only the critical buckling loads are affected, but also the slope of both central deflection and end-shortening curves. Misalignment of fillers also has a deep influence on the buckling modes as shown in Fig. 12. This fact is of crucial relevance in the design of FG-CNTRC fuselage panels. The orientation distribution of CNTs embedded in polymer matrices depends upon the manufacturing process. Unless special measures are taken, nanotubes are randomly oriented within the matrix. There exist several techniques in the literature for the aligning of the nanotubes, such as the application of high magnetic fields. However, these techniques are usually expensive and hardly scalable, so the mechanical enhancements must be properly justified. This sort of results supports the importance of developing cost-efficient aligning techniques for the development of high-performance composites.

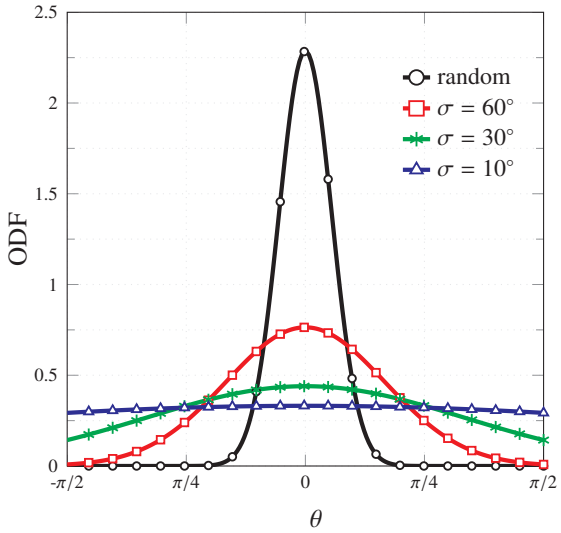

Figure 11: Orientation distribution function $\Omega(\theta)$ with different standard deviation values σ.

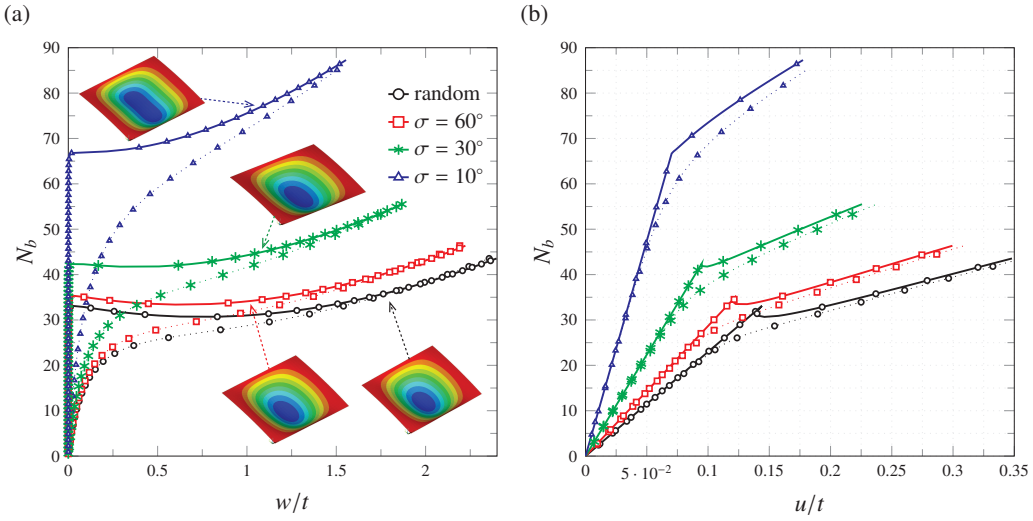

Figure 12: Non-dimensional central deflection (a) and end-shortening (b) of uniaxially compressed FG-CNTRC curved panels with CSCS boundary conditions and different SWCNT misalignment degrees (UD, a=b=1 m, t =a/50 , h =0.025b, V_c = 0.12, $\alpha = 0$). Solid and dotted lines denote the results for perfect and imperfect ($w_0 = 0.1t$) panels, respectively.

4.2.5. Effect of waviness

The effect of CNTs waviness is also studied for different spiral angles θ^w as shown in Fig. 13. As already discussed in Shi *et al.* [56], CNTs waviness induces a substantial reduction of the longitudinal effective Young's modulus, whilst transverse Young's moduli experience slight increases. It can be observed in Fig. 13(a) that spiral

angles below 80° induce substantial decreases in the critical buckling load. Similarly, it is clearly displayed in Fig. 13(b) that waviness has an important effect on the axial stiffness of the panels, and severe reductions of the slope of the equilibrium paths can be observed. In order to remark this effect, Fig. 14 shows the relative non-dimensional load factor N_b with respect to the one obtained for straight fibers, $\theta^w = 90°$, as a function of the waviness spiral angle θ^w, and registered at a non-dimensional central deflection value of $w/t = 0.5$. It can be seen that a sharp reduction is found for spiral angles between 60° and 80°. It is also worth noting the influence of CNTs waviness on the shape of the post-buckling equilibrium paths. It can be seen that for decreasing spiral angles θ^w, and thus decreasing CNTs anisotropy, the post-buckling paths exhibit a limit point and a snap-through transition regime, as it is the case for $\theta^w = 50°$. Nonetheless, as θ^w increases, the snap-though transition tends to disappear and the post-buckling paths exhibit almost bi-linear behaviors.

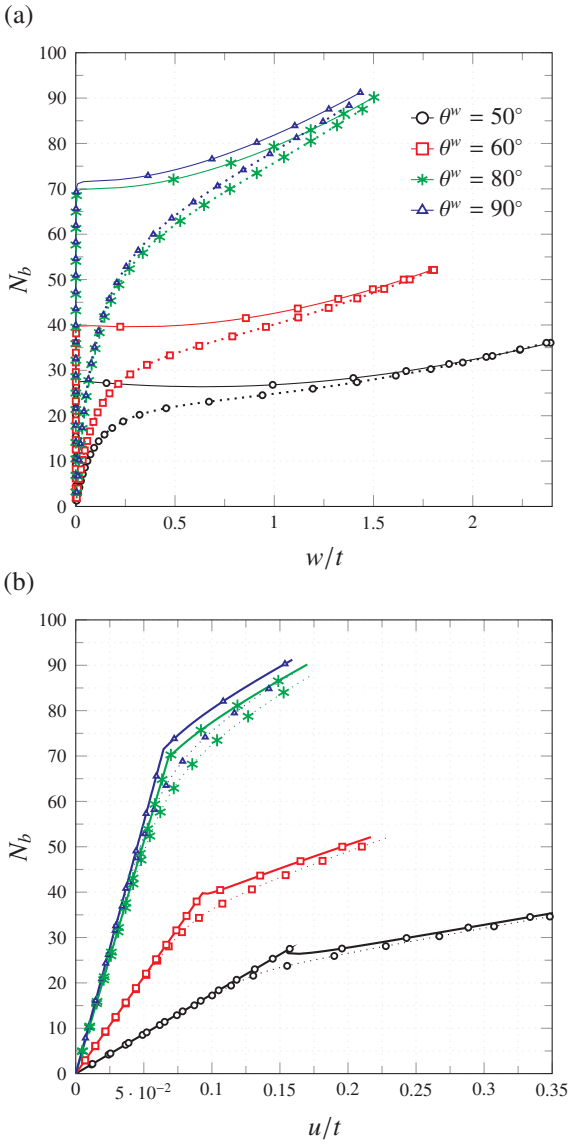

Figure 13: Non-dimensional central deflection (a) and end-shortening (b) of uniaxially compressed FG-CNTRC curved panels with CSCS boundary conditions and different degrees of CNT waviness (UD, a=b=1 m, t =a/50 , h =0.025b, $V_c = 0.12$, $\alpha = 0$). Solid and dotted lines denote the results for perfect and imperfect ($w_0 = 0.1t$) panels, respectively.

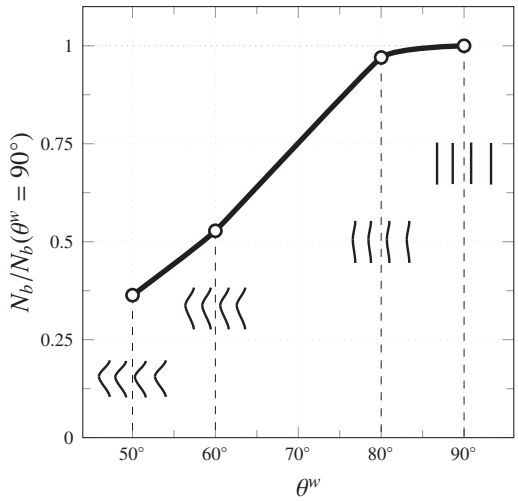

Figure 14: Relative non-dimensional load factor $N_b/N_b(\theta^w = 90°)$ versus waviness spiral angles θ^w for non-dimensional central deflection $w/t = 0.5$ (UD, a=b=1 m, t =a/50 , h =0.025b, $V_c = 0.12$, $\alpha = 0$).

4.2.6. Effect of agglomeration

Finally, the effect of agglomeration of SWCNTs is studied. To this aim, the first agglomeration parameter is fixed at ζ=0.2, and the post-buckling paths are obtained for varying ξ parameters between the limit values of 0.2 and 1. Let us recall that limit cases ζ=ξ=0.2 and ζ=0.2, ξ=1 correspond to uniform dispersions and fillers located at bundles, respectively. Fig. 15 shows the post-buckling equilibrium paths for FG-CNTRC curved panels with different agglomeration degrees and CSCS boundary condition. A first important conclusion is that agglomeration has a detrimental effect on the mechanical behavior of FG-CNTRCs. For example, in the case of the deflection of UD distribution, Fig. 15 (a), CNTs located only within the bundles (ξ=1) originates a reduction of the critical buckling load of more than three times. The same effect can be observed for all the filler distributions and, therefore, it can be concluded that agglomeration always reduces both the critical buckling load and the post-buckling stiffness. This conclusion has a pivotal importance for the design of high-performance FG-CNTRCs. Although there exist a few techniques to improve the dispersion of CNTs, achieving uniform distribution of fillers remains a challenging task. Nevertheless, as observed in these analyses, mitigating the agglomeration effects is of critical importance for the development of high strength CNT reinforced composites. Finally, it is worth noting that, as in previous analyses, the stiffest post-buckling paths are obtained for FG-X filler distributions. UD, FG-V and FG-0 distributions provide, in decreasing order, lesser critical buckling loads and non-dimensional force parameters. Therefore, the discussion on the greater efficiency of filler distributions with CNTs close to the top and bottom panel surfaces can be also made here.

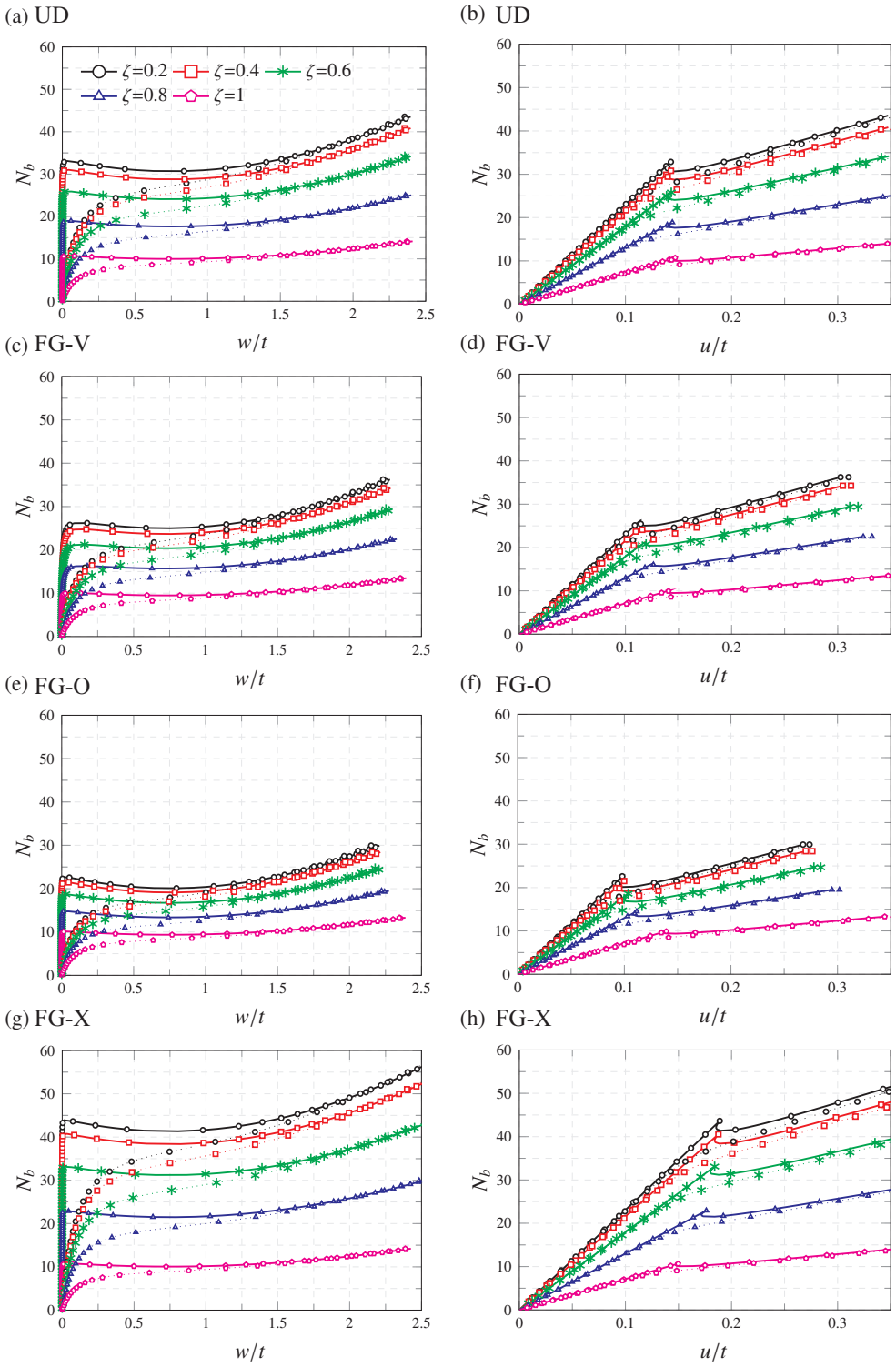

Figure 15: Non-dimensional central deflection and end-shortening of uniaxially compressed FG-CNTRC curved panels with UD, (a) and (b), FG-V (c) and (d), FG-O, (e) and (f), and FG-X, (g) and (h), SWCNT distributions (CSCS, ξ=0.2, a=b=1 m, t =a/50 , h = 0.025b, V_c = 0.12, α = 0). Solid and dotted lines denote the results for perfect and imperfect (w_0 = 0.1t) panels, respectively.

5. Conclusions

In this paper, the influence of micromechanical aspects such as fibers orientation, fibers distribution, orientation distribution of fillers, waviness and agglomeration on the post-buckling behavior of uniaxially compressed FG-CNTRC curved panels has been investigated. The panels have been modeled with the commercial FEA software ANSYS v15.0 with effective material properties estimated by means of a micromechanics model based on the Eshelby-Mori-Tanaka approach. The results show substantial influence of the analyzed variables on the post-buckling behavior of FG-CNTRC curved panels. The main findings of this research work can be summarized as follows:

- The results demonstrate that higher SWCNT contents lead to stiffer panels and, therefore, higher critical buckling loads. Limited CNTs contents have yielded substantial increases in the critical buckling loads with respect to the neat polymer. It has been shown that both axial and bending stiffness increases with CNT volume fraction and, thus, so do the slopes of both vertical deflection and end-shortening.
- It has been shown that CNTs orientation has a critical effect on the linear buckling and post-buckling behavior of FG-CNTRC panels. Fibers orientation has a deep impact on the buckling modes and, therefore, the post-buckling equilibrium paths are also heavily influenced.
- FG-V distribution has been shown initially unstable for SSSS conditions. This behavior is ascribed to the coupling between membrane and bending stiffnesses due to the asymmetry of the distribution. Conversely, it has been shown that this coupling is lost in the case of CSCS by means of rotational restraints at curved edges. In this case, the panels have been shown to exhibit typical pre- and post-buckling behavior.
- Results have shown that FG-O CNTRC cylindrical panels provide the lowest post-buckling strength, while FG-X CNTRC panels exhibit the highest one among the four studied CNT distributions. It has been concluded that CNTs distributed close to the top and bottom surfaces are more efficient in increasing the stiffness and post-buckling strength of FG-CNTRC panels than CNTs distributed near the mid-plane.
- It has been also illustrated that the orientation distribution of CNTs has a substantial effect of on the post-buckling behavior of FG-CNTRCs. The maximum buckling loads have been found for fully aligned SWCNTs configurations, and decreasing with the CNTs misalignment degree. Since the anisotropy of the resulting composite depends upon the CNTs orientation distribution, it has been shown that the overall stiffness of FG-CNTRC curved panels is highly affected by the orientation distribution of CNTs and, likewise, so are the slopes of both central deflection and end-shortening curves.
- The results have shown that the CNT waviness induces substantial reductions in the critical buckling loads as well as severe reductions of the slopes of the equilibrium paths. This behavior has been explained by the reduction of the longitudinal effective Young's modulus induced by curviness.
- It has been shown that agglomeration degrades the post-buckling strength for all the fiber distributions. Hence, agglomeration of CNTs in bundles can be understood as defects in the microstructure of the composite. These results strengthen the importance of dispersion techniques for the development of high-performance composites.

This paper is envisaged to provide valuable conclusions on the design of high performance curved panels under axial loading conditions. Furthermore, the presented micromechanics framework is aimed to be useful for the analysis of different structural elements, in which effects such as waviness or agglomeration can substantially influence the effective mechanical performance.

Acknowledgement

This work was supported by the Ministerio de Economía y Competitividad of Spain, the European Regional Development Fund and the Consejería de Economía, Innovación, Ciencia y Empleo of Andalucía (Spain) under projects DPI2014-53947-R and P12-TEP-2546. E. G-M was also supported by a FPU contract-fellowship from the Spanish Ministry of Education Ref: FPU13/04892. The financial support is gratefully acknowledged.

References

[1] J. Hale, Boeing 787 from the ground up, Aero 4 (2006) 7.

[2] J. N. Coleman, U. Khan, W. J. Blau, Y. K. Gunko, Small but strong: A review of the mechanical properties of carbon nanotube-polymer composites, Carbon 44 (2006) 1624–1652.

[3] R. F. Gibson, A review of recent research on mechanics of multifunctional composite materials and structures, Composite Structures 92 (2010) 2793–2810.

[4] A. L. Materazzi, F. Ubertini, A. D'Alessandro, Carbon nanotube cement-based transducers for dynamic sensing of strain, Cement and Concrete Composites 37 (2013) 2–11.

[5] T. Schumacher, E. T. Thostenson, Development of structural carbon nanotube–based sensing composites for concrete structures, Journal of Intelligent Material Systems and Structures 25(11) (2013) 1331–1339.

[6] F. Ubertini, A. L. Materazzi, A. D'Alessandro, S. Laflamme, Natural frequencies identification of a reinforced concrete beam using carbon nanotube cement-based sensors, Engineering Structures 60 (2014) 265–275.

[7] E. García-Macías, A. D'Alessandro, R. Castro-Triguero, D. Pérez-Mira, F. Ubertini, Micromechanics modeling of the uniaxial strain-sensing property of carbon nanotube cement-matrix composites for SHM applications, Composite Structures 163 (2017) 195–215.

[8] F. Panozzo, M. Zappalorto, M. Quaresimin, Analytical model for the prediction of the piezoresistive behavior of cnt modified polymers, Composites Part B: Engineering 109 (2017) 53–63.

[9] E. García-Macías, A. Downey, A. D'Alessandro, R. Castro-Triguero, S. Laflamme, F. Ubertini, Enhanced lumped circuit model for smart nanocomposite cement-based sensors under dynamic compressive loading conditions, Sensors and Actuators A: Physical 260 (2017) 45–57.

[10] G. Udupa, S. S. Rao, K. Gangadharan, Functionally graded composite materials: An overview, Procedia Materials Science 5 (2014) 1291–1299.

[11] N. Kharghani, C. G. Soares, Behavior of composite laminates with embedded delaminations, Composite Structures 150 (2016) 226–239.

[12] M. Nikbakht, J. Yousefi, H. Hosseini-Toudeshky, G. Minak, Delamination evaluation of composite laminates with different interface fiber orientations using acoustic emission features and micro visualization, Composites Part B: Engineering 113 (2017) 185–196.

[13] S. C. Redshaw, The elastic instability of a thin curved panel subjected to an axial thrust, its axial and circumferential edges being simply supported, HM Stationery Office, 1934.

[14] S. P. Timoshenko, J. M. Gere, Theory of elastic stability, engineering societies monographs, 1961.

[15] E. Z. Stowell, Critical compressive stress for curved sheet supported along all edges and elastically restrained against rotation along the unloaded edges, NACA RB (1943).

[16] K. Le Tran, L. Davaine, C. Douthe, K. Sab, Stability of curved panels under uniform axial compression, Journal of constructional steel research 69 (2012) 30–38.

[17] J. P. Peterson, Buckling of Stiffened Cylinders in Axial Compression and Bending: A Review of Test Data, National Aeronautics and Space Administration, 1969.

[18] R. P. Thornburgh, M. W. Hilburger, Identifying and characterizing discrepancies between test and analysis results of compression-loaded panels (2005).

[19] H. L. Cox, E. Pribram, The elements of the buckling of curved plates, The Aeronautical Journal 52 (1948) 551–565.

[20] T. Karman, The buckling of thin cylindrical shells under axial compression, Journal of the Aeronautical Sciences 8 (1941) 303–312.

[21] W. T. Koiter, The stability of elastic equilibrium, Ph.D. thesis, Techische Hooge School, Delft, 1945. (English translation NASA TT-F-10833, 1967).

[22] J. Hutchinson, W. Koiter, Postbuckling theory, Appl. Mech. Rev 23 (1970) 1353–1366.

[23] G. Pope, The buckling behaviour in axial compression of slightly-curved panels, including the effect of shear deformability, International Journal of Solids and Structures 4 (1968) 323–340.

[24] E. Riks, An incremental approach to the solution of snapping and buckling problems, International Journal of Solids and Structures 15 (1979) 529–551.

[25] M. Crisfield, A fast incremental/iterative solution procedure that handles "snap-through", Computers & Structures 13 (1981) 55–62.

[26] C. Tsai, A. Palazotto, Nonlinear and multiple snapping responses of cylindrical panels comparing displacement control and Riks method, Computers & Structures 41 (1991) 605–610.

[27] N. R. Bauld, N. S. Khot, A numerical and experimental investigation of the buckling behavior of composite panels, Computers & Structures 15 (1982) 393–403.

[28] N. S. Khot, N. R. Bauld, Further comparison of the numerical and experimental buckling behaviors of composite panels, Computers & Structures 17 (1983) 61–68.

[29] Y. Zhang, F. Matthews, Postbuckling behaviour of curved panels of generally layered composite materials, Composite Structures 1 (1983) 115–135.

[30] Y. Zhang, F. L. Matthews, Large deflection behavior of simply supported laminated panels under in-plane loading, Journal of Applied Mechanics 52 (1985) 553.

[31] E. Madenci, A. Barut, Pre- and postbuckling response of curved, thin, composite panels with cutouts under compression, International Journal for Numerical Methods in Engineering 37 (1994) 1499–1510.

[32] M. W. Hilburger, V. O. Britt, M. P. Nemeth, Buckling behavior of compression-loaded quasi-isotropic curved panels with a circular cutout, International Journal of Solids and Structures 38 (2001) 1495–1522.

[33] M. Hilburger, M. Nemeth, J. S. Jr., Nonlinear and buckling behavior of curved panels subjected to combined loads, in: 19th AIAA Applied Aerodynamics Conference, American Institute of Aeronautics and Astronautics (AIAA), 2001.

[34] M. Hilburger, J. Riddick, R. Thornburgh, M. Nemeth, Effects of elastic edge restraints and initial prestress on the buckling response of compression-loaded composite panels, in: 45th AIAA/ASME/ASCE/AHS/ASC Structures, Structural Dynamics & Materials Conference, p. 1713.

[35] S. White, G. Raju, P. Weaver, Initial post-buckling of variable-stiffness curved panels, Journal of the Mechanics and Physics of Solids 71 (2014) 132–155.

[36] H. S. Shen, C. L. Zhang, Thermal buckling and postbuckling behavior of functionally graded carbon nanotube-reinforced composite plates, Materials & Design 31 (2010) 3403–3411.

[37] P. Zhu, L. W. Zhang, K. M. Liew, Geometrically nonlinear thermomechanical analysis of moderately thick functionally graded plates using a local Petrov–Galerkin approach with moving Kriging interpolation, Composite Structures 107 (2014) 298–314.

[38] Z. Lei, L. Zhang, K. Liew, J. Yu, Dynamic stability analysis of carbon nanotube-reinforced functionally graded cylindrical panels using the element-free kp-Ritz method, Composite Structures 113 (2014) 328–338.

[39] H. S. Shen, Y. Xiang, Postbuckling of axially compressed nanotube-reinforced composite cylindrical panels resting on elastic foundations in thermal environments, Composites Part B: Engineering 67 (2014) 50–61.

[40] L. W. Zhang, K. M. Liew, J. N. Reddy, Postbuckling of carbon nanotube reinforced functionally graded plates with edges elastically restrained against translation and rotation under axial compression, Computer Methods in Applied Mechanics and Engineering 298 (2016) 1–28.

[41] H. S. Shen, Y. Xiang, F. Lin, D. Hui, Buckling and postbuckling of functionally graded graphene-reinforced composite laminated plates in thermal environments, Composites Part B: Engineering 119 (2017) 67–78.

[42] H. S. Shen, Nonlinear bending of functionally graded carbon nanotube-reinforced composite plates in thermal environments, Composite Structures 91 (2009) 9–19.

[43] L. W. Zhang, K. M. Liew, Postbuckling analysis of axially compressed CNT reinforced functionally graded composite plates resting on Pasternak foundations using an element-free approach, Composite Structures 138 (2016) 40–51.

[44] L. W. Zhang, Y. Zhang, G. L. Zou, K. M. Liew, Free vibration analysis of triangular CNT-reinforced composite plates subjected to in-plane stresses using FSDT element-free method, Composite Structures 149 (2016) 247–260.

[45] E. García-Macías, R. Castro-Triguero, E. I. S. Flores, M. I. Friswell, R. Gallego, Static and free vibration analysis of functionally graded carbon nanotube reinforced skew plates, Composite Structures 140 (2016) 473–490.

[46] E. García-Macías, R. Castro-Triguero, M. I. Friswell, S. Adhikari, A. Sáez, Metamodel-based approach for stochastic free vibration analysis of functionally graded carbon nanotube reinforced plates, Composite Structures 152 (2016) 183–198.

[47] M. Mohammadimehr, S. Shahedi, High-order buckling and free vibration analysis of two types sandwich beam including al or pvc-foam flexible core and cnts reinforced nanocomposite face sheets using gdqm, Composites Part B: Engineering 108 (2017) 91–107.

[48] A. Allaoui, S. Bai, H. Cheng, J. Bai, Mechanical and electrical properties of a MWNT/epoxy composite, Composites Science and Technology 62 (2002) 1993–1998.

[49] J. M. Wernik, S. A. Meguid, Recent developments in multifunctional nanocomposites using carbon nanotubes, Applied Mechanics Reviews 63 (2010) 050801.

[50] M. S. P. Shaffer, A. H. Windle, Fabrication and characterization of carbon nanotube/poly(vinyl alcohol) composites, Advanced Materials 11 (1999) 937–941.

[51] B. Vigolo, Macroscopic fibers and ribbons of oriented carbon nanotubes, Science 290 (2000) 1331–1334.

[52] R. H. Poelma, X. Fan, Z. Y. Hu, G. Van Tendeloo, H. W. van Zeijl, G. Q. Zhang, Effects of nanostructure and coating on the mechanics of carbon nanotube arrays, Advanced Functional Materials 26 (2016) 1233–1242.

[53] E. García-Macías, A. D'Alessandro, R. Castro-Triguero, D. Pérez-Mira, F. Ubertini, Micromechanics modeling of the electrical conductivity of carbon nanotube cement-matrix composites, Composites Part B: Engineering 108 (2017) 451–469.

[54] T. Mori, K. Tanaka, Average stress in matrix and average elastic energy of materials with misfitting inclusions, Acta metallurgica 21 (1973) 571–574.

[55] F. Tornabene, N. Fantuzzi, M. Bacciocchi, E. Viola, Effect of agglomeration on the natural frequencies of functionally graded carbon nanotube-reinforced laminated composite doubly-curved shells, Composites Part B: Engineering 89 (2016) 187–218.

[56] D. Shi, X. Feng, Y. Y. Huang, K. Hwang, H. Gao, The effect of nanotube waviness and agglomeration on the elastic property of carbon nanotube-reinforced composites, Journal of Engineering Materials and Technology 126 (2004) 250–257.

[57] F. Tornabene, N. Fantuzzi, M. Bacciocchi, Linear static response of nanocomposite plates and shells reinforced by agglomerated carbon nanotubes, Composites Part B: Engineering (2016).

[58] L. W. Zhang, L. Xiao, Mechanical behavior of laminated CNT-reinforced composite skew plates subjected to dynamic loading, Composites Part B: Engineering (2017).

[59] B. Sobhaniaragh, M. Nejati, W. J. Mansur, Buckling modelling of ring and stringer stiffened cylindrical shells aggregated by graded cnts, Composites Part B: Engineering (2017).

[60] M. Talò, B. Krause, J. Pionteck, G. Lanzara, W. Lacarbonara, An updated micromechanical model based on morphological characterization of carbon nanotube nanocomposites, Composites Part B: Engineering 115 (2017) 70–78.

[61] S. Kamarian, M. Salim, R. Dimitri, F. Tornabene, Free vibration analysis of conical shells reinforced with agglomerated carbon nanotubes, International Journal of Mechanical Sciences 108 (2016) 157–165.

[62] B. Sobhaniaragh, R. C. Batra, W. J. Mansur, F. C. Peters, Thermal response of ceramic matrix nanocomposite cylindrical shells using eshelby-mori-tanaka homogenization scheme, Composites Part B: Engineering 118 (2017) 41–53.

[63] M. S. Al-Haik, H. Garmestani, D. S. Li, M. Y. Hussaini, S. S. Sablin, R. Tannenbaum, K. Dahmen, Mechanical properties of magnetically oriented epoxy, Journal of Polymer Science Part B: Polymer Physics 42 (2004) 1586–1600.

[64] E. García-Macías, L. Rodríguez-Tembleque, R. Castro-Triguero, A. Sáez, Buckling analysis of functionally graded carbon nanotube-reinforced curved panels under axial compression and shear, Composites Part B: Engineering 108 (2017) 243–256.

[65] S. Nemat-Nasser, M. Hori, Micromechanics: overall properties of heterogeneous materials, volume 37, Elsevier, 2013.

[66] J. D. Eshelby, The determination of the elastic field of an ellipsoidal inclusion, and related problems, Proceedings of the Royal Society of London. Series A. Mathematical and Physical Sciences 241 (1957) 376–396.

[67] J. Eshelby, The elastic field outside an ellipsoidal inclusion, Proceedings of the Royal Society of London. Series A, Mathematical and Physical Sciences (1959) 561–569.

[68] Y. Benveniste, A new approach to the application of Mori-Tanaka's theory in composite materials, Mechanics of materials 6 (1987) 147–157.

[69] T. Mura, Micromechanics of defects in solids, volume 3, Springer, 1987.

[70] R. Hill, A self-consistent mechanics of composite materials, Journal of the Mechanics and Physics of Solids 13 (1965) 213–222.

[71] J. Schjødt-Thomsen, R. Pyrz, The Mori-Tanaka stiffness tensor: diagonal symmetry, complex fibre orientations and non-dilute volume fractions, Mechanics of Materials 33 (2001) 531–544.

[72] H. Li, H. Xiao, J. Yuan, J. Ou, Microstructure of cement mortar with nano-particles, Composites Part B: Engineering 35 (2004) 185–189.

[73] Structural analysis guide, Release 15.0, ANSYS Inc, Cannonsburg, PA (2014).

[74] B. W. Forde, S. F. Stiemer, Improved arc length orthogonality methods for nonlinear finite element analysis, Computers & Structures 27 (1987) 625–630.

[75] E. Efraim, M. Eisenberger, Exact vibration analysis of variable thickness thick annular isotropic and FGM plates, Journal of Sound and Vibration 299 (2007) 720–738.

[76] V. Popov, V. Van Doren, M. Balkanski, Elastic properties of crystals of single-walled carbon nanotubes, Solid State Communications 114 (2000) 395–399.

[77] N. Yamaki, Postbuckling behavior of rectangular plates with small initial curvature loaded in edge compression—(continued), Journal of Applied Mechanics 27 (1960) 335.

[78] N. Yamaki, Experiments on the postbuckling behavior of square plates loaded in edge compression, Journal of Applied Mechanics 28 (1961) 238.

[79] K. Liew, Z. Lei, J. Yu, L. Zhang, Postbuckling of carbon nanotube-reinforced functionally graded cylindrical panels under axial compression using a meshless approach, Computer Methods in Applied Mechanics and Engineering 268 (2014) 1–17.

[80] A. M. Esawi, M. M. Farag, Carbon nanotube reinforced composites: potential and current challenges, Materials & Design 28 (2007) 2394–2401.

[81] J. Fidelus, E. Wiesel, F. Gojny, K. Schulte, H. Wagner, Thermo-mechanical properties of randomly oriented carbon/epoxy nanocomposites, Composites Part A: Applied Science and Manufacturing 36 (2005) 1555–1561.

[82] B. Sobhani Aragh, A. Nasrollah Barati, H. Hedayati, Eshelby-Mori-Tanaka approach for vibrational behavior of continuously graded carbon nanotube-reinforced cylindrical panels, Composites Part B: Engineering 43 (2012) 1943–1954.